DETERMINING THE ELECTRONIC PROPERTIES OF SURFACE ENHANCED RAMAN SPECTROSCOPY SUBSTRATES

by

©Liam David Whelan, B.Sc.

A thesis submitted to the School of Graduate Studies in partial fulfillment of the requirements for the degree of

Master of Science

Department of Chemistry

Memorial University of Newfoundland

April 2015

St. John's Newfoundland

Abstract

Surface Enhanced Raman Spectroscopy (SERS) is an ultra-sensitive technique for optical detection of target analytes. Our work focuses on detecting oil in water using SERS, with this thesis using phenanthrene as a model compound. SERS is a technique which takes advantage of the optical properties of metal substrates to greatly increase the intensities of adsorbed analytes' vibrational modes. The rapid development of novel materials as SERS active substrates requires an efficient screening method. SERS Enhancement Factor (EF) does correlate somewhat with surface morphology and UV-Vis absorption, however we present a technique which shows an even stronger correlation and is ultimately a better screening tool: Kelvin Probe Force Microscopy (KPFM). This technique maps the electronic properties of a substrate to its surface morphology. This thesis covers two classes of SERS substrates: annealed bimetallic systems and nanosphere patterned mono- and bimetallic systems. The ability to directly map the electronic properties of a substrate to its morphological properties is of critical importance in determining a key link between the macroscale SERS sensor response and the microscale substrate structure. Our major findings indicate that when Au/Cr nanostructured films' work function is near the calculated and experimental values for the HOMO-LUMO gap of the target analyte, phenanthrene, the observed SERS intensity reaches a maximum.

Acknowledgements

I must first acknowledge my supervisor, Dr. Erika Merschrod for her years of support to me. Her ability to provide guidance was not only limited to scientific concerns but to my personal concerns as well which I am forever indebted to her for. I would like to also thank Dr. Celine Schneider for giving me an opportunity where many would likely not. This work would not have been possible without the support and love from my wonderful partner Alison who spent countless evenings listening to me whine and steering me in the correct direction when I was off course. I need to thank my wonderful parents, Joan and Gerry, and my sister Holly who supported, encouraged and believed in me the entire time (and oh so much more, but I suspect that's beyond the context of this thesis work!) I would also like to acknowledge my friends Lucas, Josh, Teles, Doug, Kerri, Abhi and all the others I'm forgetting (sorry!) for all the help and friendship. This would have been far more difficult without your help and I'm eternally grateful. I need to thank the rest of the Merschrod group for providing attentive ears and ideas to me throughout the years. I would also like to acknowledge MUN SGS, NSERC, PRNL, RDC, ACOA (AIF), and CFI for the funding over the years.

Table of Contents

List of Tables

List of Figures

Chapter 1

Introduction to Surface Enhanced Raman Spectroscopy

1.1 Raman Spectroscopy

Raman spectroscopy is a vibrational spectroscopic technique that takes advantage of inelastic scattering of incident radiation [1]. Modern day Raman spectroscopy is a highly accurate and robust analytical vibrational spectroscopic method and is used in all manner of research and industrial applications, from optoelectronics [2] to archaeological specimens [3], priceless works of art [4], and biological samples [5]. This is due in part to its high specificity and the fact it is a non-destructive properties. Furthermore, Raman spectroscopy is not limited to a certain phase of material and can be readily employed to analyze gaseous [6], liquid [7], or solid [8] materials. As this technique involves observation of vibrational modes of the molecules present in a sample, this technique is becoming more important to chemists, materials scientists, and physicists as it provides information such as surface adsorption behavior [9], all with a high degree of specificity due to the characteristic "finger print" nature of the

observed Raman spectra.

1.1.1 History of Raman Spectroscopy

Raman spectroscopy's namesake comes from one of its discoverers, Sir Chandrasekhara Venkata Raman, who discovered Raman scattering in 1928 and was awarded the Noble prize in physics for his discovery in 1930. This scattering effect was first theorized in 1923 by Smekal and was discovered experimentally when Raman and his colleague Krishnan observed that when sunlight passed through a monochromatic filter and struck a subsequent blocking filter, some light managed to pass through this blocking filter [10]. This implies then that as the sunlight passed through the first filter (which only allowed light of a certain wavelength through) the light that made it through the second filter must have experienced a change in wavelength and could pass through this filter. This concept was later developed by Czechoslovakian George Placzek who would perform Raman measurements using a Hg arc lamp as a light source and initially using photographic detection methods [11].

Due to the low sensitivity of these techniques (due in part to the light sources used), Raman spectroscopy fell into relative disuse throughout most of the 20th century where IR spectroscopic systems experienced more technological advancements. These advancements resulted in more accurate and sensitive detection of vibrational modes [12] when compared to Raman spectroscopy. With the discovery of the laser in the mid 1960's, the field of Raman spectroscopy was reinvigorated due to how common powerful laser sources became. Modern Raman spectroscopy employs more advanced optical systems such as sophisticated filters and charge-coupled device (CCD) detectors. Commonly these systems are coupled to a microscope which further enhances the power of this technique in that measuring an area of <2 μm^2 is achievable.

1.1.2 Origin of Raman Effect

The Raman effect, in simplest terms, describes the inelastic scattering behavior of light as discovered by Raman and Krishnan in 1928 [10]. Specifically, it is when a molecule experiences some incident light radiation (i.e. laser radiation) and is excited from its ground state to a virtual excited state. Upon relaxation from this excited state, a photon is emitted and the system transitions to a new vibrational state. This change in vibrational states in the molecule causes the emitted photon's frequency to shift away from the excitation wavelength and this shift is ultimately what is detected in the Raman spectroscope [1]. It is important to make the distinction here that Raman scattering involves photonic excitation from the ground state to a virtual excited state, whereas fluorescence or infrared absorption events involve an excitation to a discrete excited state [1]. Figure 1.1 has been adapted from G. L. Eesley's text [13] and depicts the three significant forms of light scattering.

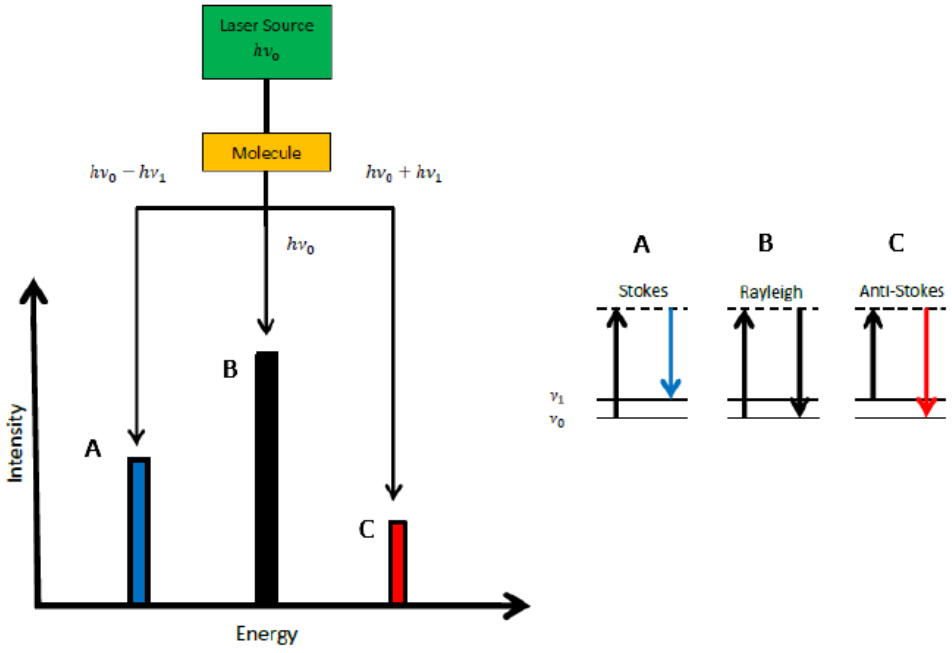

Figure 1.1: Schematic diagram of molecular light scattering – Stokes, Rayleigh, and anti-Stokes scattering. Adapted from [13]

As Figure 1.1 depicted there are three major forms of light scattering: Stokes scattering, Rayleigh scattering, and anti-Stokes scattering. Of these, Stokes and anti-Stokes scattering are collectively considered as Raman scattering [1]. Relative intensities of the Stokes and anti-Stokes events are based on the fact that the number of molecules in each state follow a standard Boltzmann distribution, implying that the lower energy conformation will be statistically more intense [1]. Rayleigh (elastic) scattering is the simplest of the three – this is where the expelled photon's frequency matches the incident radiation's frequency. This is shown in the lower center inset, where the system is excited from ν_0 to a virtual excited state and relaxes along the same pathway, returning to ν_0.

Stokes scattering is the second most likely event that occurs which is where the molecule is excited from the ground state and relaxes to a discrete vibrational excited state. This transition results in light scattered at lower energy than the Rayleight light, as per Figure 1.1 and can be expressed by $h\nu_0$ - $h\nu_1$. The third scattering event is called anti-Stokes scattering and this is where scattering occurs from an excited vibrational state ν_1 to the virtual excited state. This is followed by a relaxation event to the vibrational ground state, ν_0. This transition can be mathematically described by the following: $h\nu_0 + h\nu_1$. Raman spectroscopy relies on detecting "shifted" spectral lines, specifically Stokes and anti-Stokes scattering events. For this reason, Raman sensitivity can be quite low as elastic Rayleigh scattering makes up the majority of the detected scattering [14]. The vibrational and rotational properties of the molecule can be determined from this scattered photon [1].

1.1.3 Polarizability of a molecule

The polarizability of a molecule is a response to an electric field [1]. Given the correct conditions positively charged nuclei within the molecule are attracted by the negative

pole of the field and this results in an induced dipole moment within the molecule [1]. This induced dipole moment is expressed by Eqn 1.1:

$$\mu = \alpha E \tag{1.1}$$

where μ refers to the magnitude of the induced dipole moment, α is the polarizability of the molecule, and E is the magnitude of the electric field. In the case where a molecule experiences a oscillating electric field, as from incoming radiation, this electric field induces an oscillating polarization in the molecule. This induced polarizibility gives rise to Raman specific active modes which can reveal information regarding the rotational and vibrational modes of the molecule which are not observable *via* infrared spectroscopy. Raman activity arises because of the induced polarizibility and is the basis of the spectroscopic technique [1]. This is demonstrated in Eqn 1.2.

$$I \propto \left(\frac{\partial \alpha}{\partial Q}\right)^2 \tag{1.2}$$

where I is Raman intensity, α is polarizibility, and Q is the coordinate of any particular vibrational mode. This relationship demonstrates that the degree of polarizibility of a molecule is directly proportional to its Raman intensity.

1.1.4 Selection rules for Raman spectroscopy

All molecules contain a number of ways in which they can vibrate, however not all vibrations are necessarily Raman active [1]. The ways in which molecules can move are defined as normal modes and can be used to describe the various ways in which the molecule can vibrate. Normal modes are also associated with specific symmetries as per group theory which in turn allows us to determine whether or not the normal

mode will be Raman active [15]. To determine the number of vibrational modes that a molecule possesses, we must consider two specific cases: linear molecules or non-linear molecules.

1.1.4.1 Non-linear case

The number of normal modes for a linear molecule can be determined by the degrees of freedom (DOF) a molecule possesses in 3D space [1]. In the non-linear case, the number of vibrational modes can be calculated by 3N-6, where N = number of atoms present in the molecule. If we consider a simple tetrahedral system, such as CH_4, we find that DOF = 3(5) - 6 = 9. This means that there are 3 translational degrees of freedom (true for any object in 3D space), 3 rotational degrees of freedom (only true for a non-linear system) and the remaining 3 degrees of freedom are normal vibrational modes for the system [16].

1.1.4.2 Linear case

Determining the number of DOF that a linear molecule has is similar to the case of the non-linear system. There is one small difference which is reflected by its equation: 3N-5. The reason why we subtract 5 degrees of freedom as opposed to 6 as per the non-linear case is due to the fact that in a linear system there are fewer rotational degrees of freedom. Specifically, the interaxial rotation is meaningless in the linear case which results in only 2 rotational DOF. For this reason, the equation for the number of vibrational DOF has been altered to reflect this, hence DOF = 3N - 5. Considering the simple linear system of a CO_2 molecule, we see that DOF = 3(3) - 5 = 4, or 4 vibrational DOF [16].

1.1.5 Raman spectroscopy sensitivity

Raman spectroscopy is a highly specific analytical technique with a number of key applications [17–19]; however there is one key drawback to this technique. As this process involves the aforementioned scattering events, sensitivity is typically quite low as this technique relies on the aforementioned shifted scattering lines, namely Stokes and anti-Stokes scattering lines. The consequence of this is that measuring low concentration samples can be quite difficult and requires highly specific experimental conditions and instrumentation [20]. The advent of surface enhanced Raman spectroscopy (SERS) has greatly reinvigorated the field of Raman spectroscopy as it overcomes some of the challenges that the low sensitivity of traditional Raman spectroscopy presents [19].

1.2 Surface Enhanced Raman Spectroscopy (SERS)

Surface enhanced Raman spectroscopy (SERS) has been a rapidly developing field of Raman spectroscopy in recent years due to the enhanced sensitivity afforded by this technique. In modern usage, it is being developed as targeted biosensors, oil-in-water sensors, and a variety of other sensing technologies. Discovered in 1974 by Fleischmann *et al.* [21], and further developed by Van Duyne [22] and Albrecht [23], the basic premise of a SERS substrate is as follows: a Raman active compound is adsorbed onto a coinage metal (classically these are Ag and Au) and then is analysed *via* standard Raman spectroscopic methods. The SERS substrate can greatly enhance the observed Raman spectra of the adsorbed analyte where enhancement factors of 10^{10} and 10^{11} have been observed over traditional Raman spectroscopy [19]. It has been demonstrated that SERS can be used to detect a single molecule as a result of the significant degree of observed enhancement [22].

1.2.1 Origin of SERS

SERS was discovered, like many things in science, seemingly by accident by Fleischmann *et al.* [21] While working in the lab late one evening, Fleischmann's postdoctoral fellow James McQuillan, was experimenting with electrochemically roughened Ag electrodes [21]. They discovered that when exposed to pyridine and analyzed *via* Raman spectroscopy, the intensity of the observed pyridine bands in system were significantly higher than expected [21]. It was suggested that this could be due to the increased surface area presented by the electrochemically roughened surface. This was later challenged independently by two research groups: Albrecht [23] and Van Duyne [24] both in 1977. Van Duyne theorised that there was an electromagnetic (EM) contribution due to the delocalized electron oscillations on the metal surface [24]. These surface electron oscillations are referred to as surface plasmons. Creighton theorized that there is a chemical interaction (charge transfer, CT) event that occurs between the substrate and analyte that corresponds to an increase in signal intensity [23]. Both theories are heavily supported in the literature and ultimately both result in the overall SERS effect [22].

1.2.2 SERS Mechanisms

There exist two significant contributions to the SERS effect: the EM enhancement effect [23] and the CT enhancement effect [24]. These two effects explain the significant enhancements observed during a SERS experiment, with the EM effect corresponding to an increase in intensity of up to 10^5 [22] and when combined with the CT effect an enhancement up to 10^{15} or single molecule detection [25].

1.2.2.1 Electromagnetic effect

The EM effect was first published by Jeanmaire and Van Duyne *et al.* in 1977 [24] as a plausible explanation for the observed enhancements of the SERS phenomena. The EM effect is described as the enhancement of the scattering of photons from an adsorbed material due to the excitation of local surface plasmons of the metal substrate due to incident light. This results in localized surface plasmon resonance (LSPR) and is the cause for significant electromagnetic field enhancement on the nanostructured material [26]. Due to the requirement for the material to absorb at the wavelength of the laser source, Au and Ag are typically employed due to their visible and near IR plasmon absorptions [27]. Other classes of metal materials have been explored extensively as the ability to tune the absorbance of the material to a wide variety of wavelengths continues to develop [28, 29]. The EM effect contributes a significant portion of the observed enhancement related to the SERS effect, although the CT effect can also play a significant role in terms of increasing the intensity observed during SERS.

1.2.2.2 Chemical effect

Creighton and Albrecht [23] published the charge transfer (CT) effect for SERS enhancement in 1977, the same year as the competing EM effect suggested by Van Duyne *et al.* It has been suggested that while the EM effect plays a significant role in explaining the SERS phenomena, it is not sufficient in justifying the significant enhancement observed in specific cases [30]. This increase in intensity is due to chemisorption between analyte and substrate. Typically, this is due to a lone pair of electrons present on the adsorbate which are donated to the substrate as suggested by Albrecht when observing pyridine's increase in intensity when adsorbed to a roughened Ag electrode [23]. An otherwise energetically inaccessible transition from an

adsorbed molecule's HOMO to its LUMO occurs due to the metal substrate behaving as a charge transfer intermediate. Figure 1.2 represents a typical energy level depiction of this charge transfer between adsorbate and metal substrate.

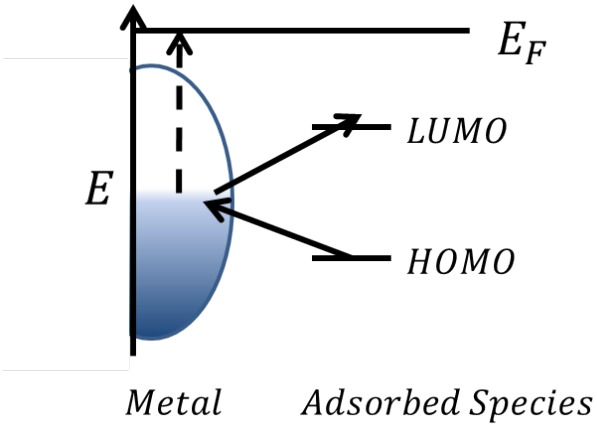

Figure 1.2: Typical energy level diagram of charge transfer between adsorbed molecule and metal substrate. E_F indicates the Fermi level of the metal.

This charge transfer results in a strong interaction between the absorbed molecule and the substrate and is the underlying mechanism behind the CT effect. It is agreed now in the literature that the CT effect occurs in concert with the EM effect, and ultimately both contribute to the overall SERS mechanism [22].

1.2.3 Current state of SERS substrates

The study of SERS has exploded in recent years with many groups racing to develop new substrates with a wide array of applications. Since 2000, there has been approximately 16000 publications on SERS (CAPLUS database) in general with a significant exponential growth in publications starting in 2000 at 317 publications until 2013 and 2014 where approximately 1900 papers were published annually. Figure 1.3 illustrates the field's rapid growth.

In the field itself, there are incredibly diverse subfields where the focus is split

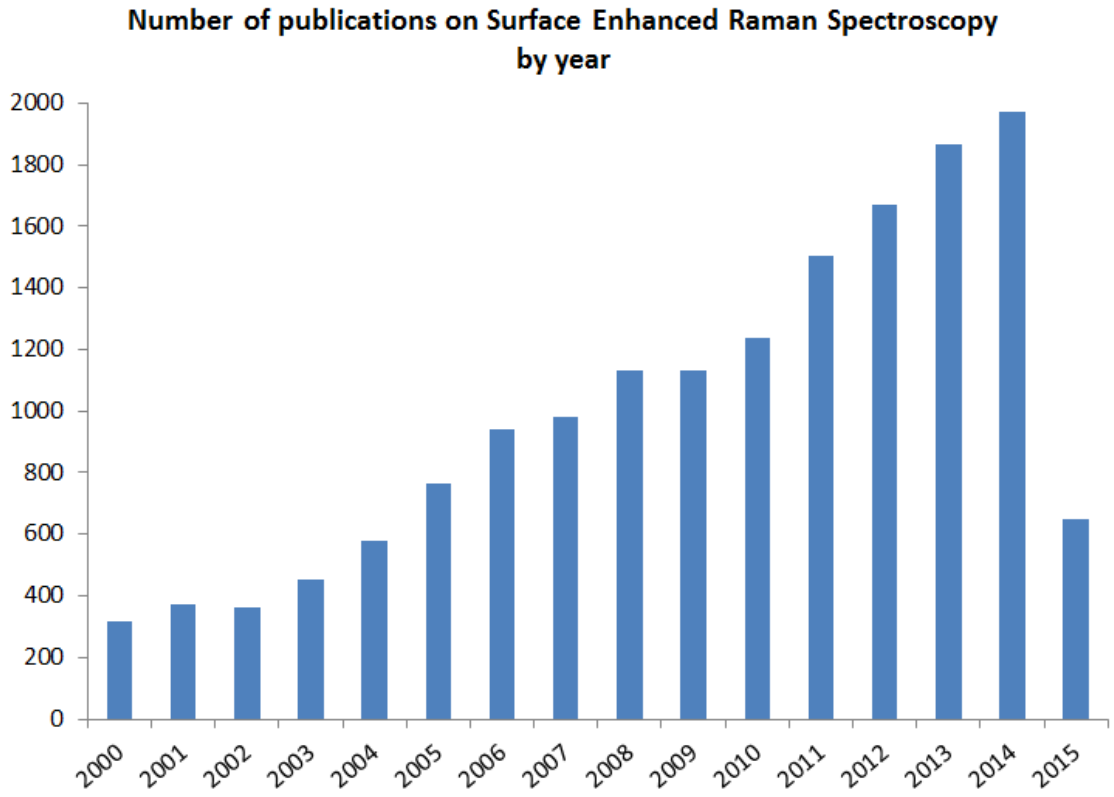

Figure 1.3: Publications by year on Surface Enhanced Raman Spectroscopy (SERS) (CAPLUS database, obtained on 5/3/2015)

between the design of the substrates themselves and the specific analyte sensing applications of known substrates. This thesis will briefly summarize the current state of bimetallic system design and the detection of polycyclic aromatic hydrocarbons (PAH's) as motivation for the work presented in this thesis.

1.2.3.1 PAH detection with SERS substrates

The detection of PAH's has been the focus of many research groups due to the environmental and industrial concerns related to PAH contamination in marine environments as a result of oil and gas exploration. Research groups such as Sanchez-Cortes [31–33], Kronfeldt [34–36] and others [37–40] have been recently pursuing this topic using SERS as a detection method. A variety of methods are employed such as using hydrophobic porous polymers decorated with gold nanoparticles (AuNP's) [41] to determine the presence of a number of key PAH's, including phenanthrene which serves as the target molecule of this thesis.

Zhao's group in particular investigated the use of "Three-dimensional superhydrophobic SERS substrates" [37] for investigating PAH systems. This was performed by producing AuNP's which were encapsulated in a Ni foam structure which contained long-chain alkyl mercaptan molecules. This foam was then treated with 1-octadecanethiol which would further increase the hydrophobicity of the foam. This resulted in a porous, superhydrophobic structure which was theorized to result in positive interactions between the target molecule of the study, pyrene, and the substrate itself.

Figure 1.4 demonstrates the response of their substrate to pyrene at a variety of concentrations. It is noted that as the concentration of pyrene increases, the SERS intensity increases as well. The standard deviation of the intensity increases as the concentration decreases, showing that from measurement to measurement on the sub-

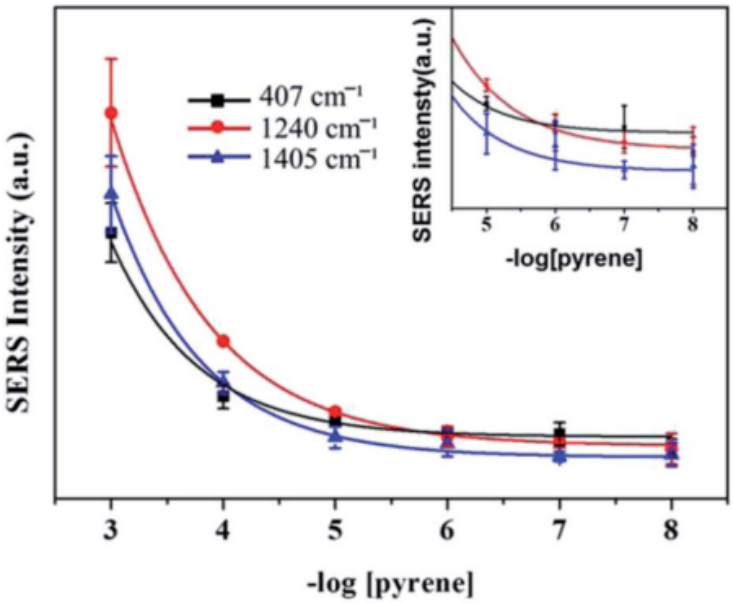

Figure 1.4: SERS intensity observed at 1405, 1240, and 407 cm^{-1} versus a range of pyrene concentrations. Reproduced from [37] with permission of The Royal Society of Chemistry.

strate there is indeed some variability and this may be due in part to the heterogeneity of the surface. This suggests that the morphology of the substrate plays a critical role to the reproducibility of the SERS measurements from experiment to experiment. Determining the precise nature of the interaction between morphology and substrate is a key motivation of the work in this thesis. This variability from sample to sample places a critical importance on the design of the substrate itself, which is the major focus of many groups in the field of SERS research.

1.2.3.2 Bimetallic SERS substrate design

The field of SERS research is dedicated in numerous ways to design SERS systems with specific functionality. A relatively straight forward way to introduce functionality within a SERS substrate is to design the substrate with mixed metals such that one metal behaves as the SERS sensing medium (classically Au) and the other exhibits

some specific functionality to attract the target molecule. Recently, groups such as Vo-Dinh's [42–44], Olivo [45, 46], Pasquale [47] and Han's [48]. The other advantage of studying these mixed metal systems is that the inclusion of multiple metals induces changes in the morphological properties of the substrate which in turn can alter the spectroscopic behavior of the system.

Recently, Vo-Dinh's group investigated Au nanostars (AuNS) as a biosensing substrate to be injected into living tissue for various *in vitro* applications [42]. The purpose of this study was to seek the highest signal using the nanostar geometry. The advantage of this type of geometry is that hot spot generation is isolated to the nanoparticle rather than requiring aggregated nanoparticles. They prepared AuNS's with Ag trapped within the structure by slowly growing AuNS's with $AgNO_3$ present in the seed solution. They employed a carbocyanine molecule as their proof of concept analyte for this study, and their results indicate that the inclusion of Ag in their system significantly affects the observed intensity. These Raman results and the TEM micrographs of both the AuNS's and AuNS@Ag are depicted in Figure 1.5.

It is observed that the incorporation of Ag into the structure of the Au nanostar induces a significant increase in SERS intensity observed. The authors explain this phenomenon by the fact that inclusion of the Ag blue shifts the substrate's plasmon to be closer to the incident laser wavelength and that by adjusting the silver thickness this blueshift was tunable.

The strategy of the work performed in this thesis is that by systematically adjusting the aggregation of the SERS active metal *via* annealing, a similar effect can be achieved. The tunability of a SERS substrate is also a key consideration when designing substrates as this allows for overall greater intensity, and subsequently allows for lower detected concentrations of analyte. The previously mentioned paper [42] also suggests that the morphology of the substrate can play a key role in terms of

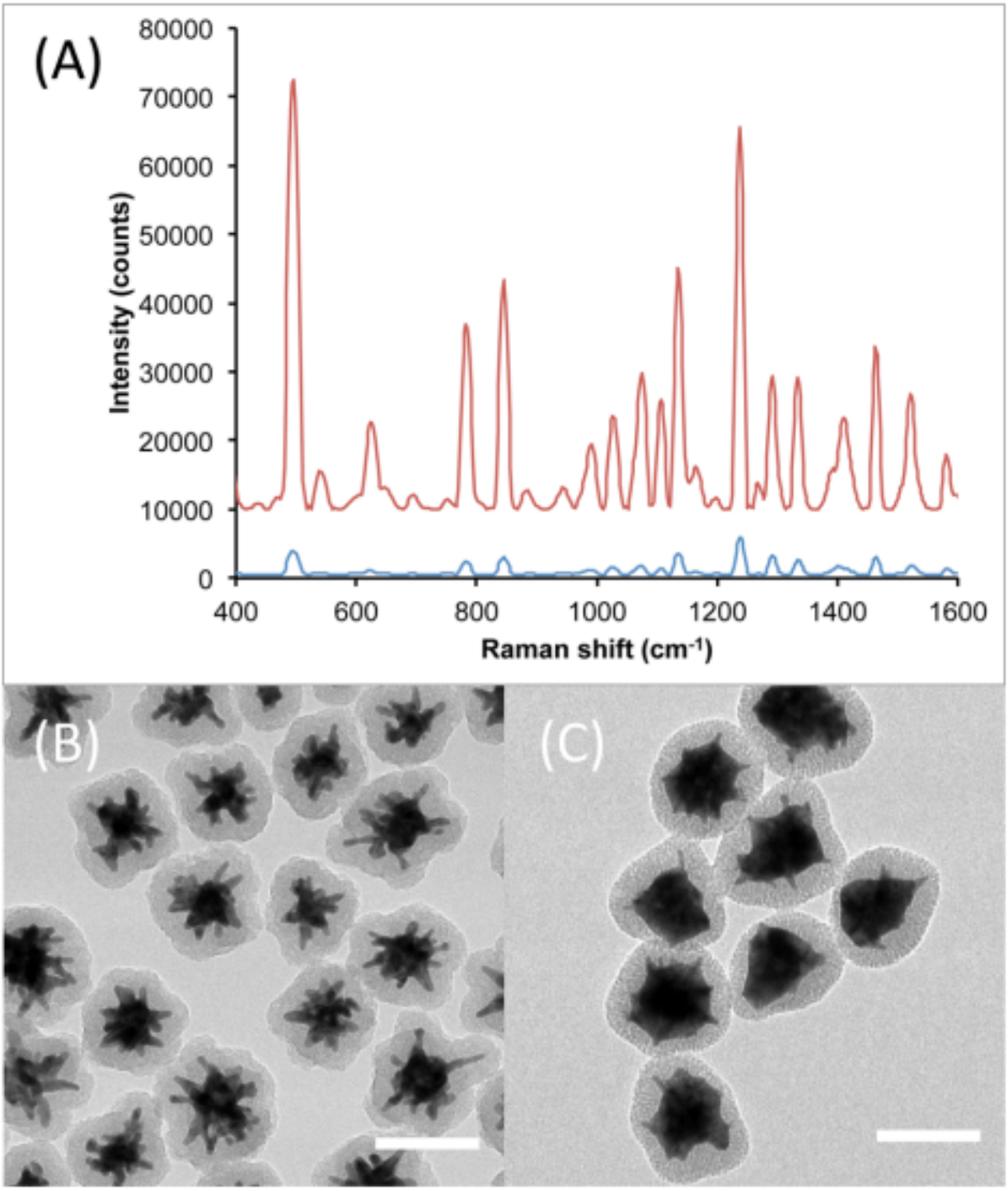

Figure 1.5: A comparison of the SERS spectra of AuNS (red) and AuNS@Ag (blue). TEM micrographs of AuNS (B) and AuNS@Ag (C) are depicted below. Scale bars are 100 nm. Reproduced from [42] with permission of The American Chemical Society.

how viable the SERS substrate is and employed TEM to determine this. The strategy presented in this thesis is that the morphological properties of the substrate can be determined *via* atomic force microscopy (AFM) with the added advantage of being able to determine the electronic properties of the substrates *via* the analogous technique of Kelvin probe force microscopy (KPFM.)

Chapter 2

Introduction to Scanning Probe Microscopy

2.1 Atomic Force Microscopy

The invention of the atomic force microscope (AFM) by Binnig *et al.* [49] revolutionized the field of materials research. The basic AFM experiment involves a nanometer scale tip interacting with a surface with highly sensitive electronics monitoring and controlling these interactions. Figure 2.1 depicts a diagram of a standard AFM experimental setup. As this method relies on a nanoscale tip interacting with the surface of interest, the technique allows for accurate and sensitive measurements of materials at length scales far below the diffraction limit of optical based techniques [49]. The tip typically has a radius ranging from 5 to 25 nm and is mounted on a cantilever composed of Si and coated with a reflective material for accurate detection of cantilever movements.

In a typical AFM experiment, a laser beam is directed towards the backside of a cantilever which can be coated with a reflective material. The laser beam is then

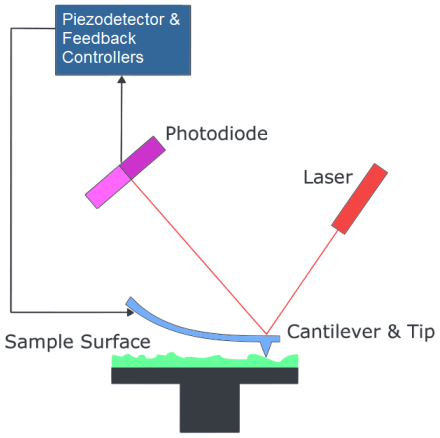

Figure 2.1: Diagram of typical AFM experiment. Reproduced under Public Domain from Wikimedia Commons

reflected onto a photodiode detector, as depicted in Figure 2.2. The AFM cantilever undergoes a raster scan along the substrate, scanning along the sample in one (x) direction and returning in the opposite direction ($-x$) to its point of origin. The tip is then offset along the perpendicular direction (y) to begin scanning the next line on the sample, as dictated by the user defined image size and resolution. This movement along the x and y axes is controlled by a piezoelectric actuator with precise control [50] at the length scales measured during a typical AFM experiment.

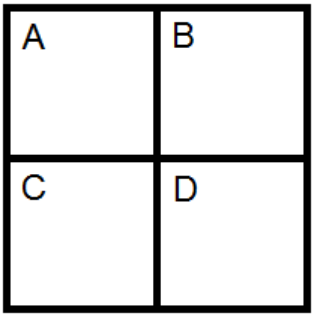

Figure 2.2: Schematic representation of AFM's photodiode sensor used for detecting laser deflection off rear of the cantilever. Adapted from NT-MDT [51]

As the tip interacts with the surface the flexible cantilever will bend and flex in response to various attractive or repulsive surface interactions (for example, electro-

static or van der Waals' forces [52]. As the cantilever bends/flexes with response to the surface, the laser beam directed at the rear of the cantilever will change angles. This laser beam can then be measured using the photodiode sensor to determine tip deflection. The photodiode detector used during AFM experiments is depicted in Figure 2.2, and the intensity of the deflection of the laser beam is expressed in Eqn 2.1. The deflection of the laser beam in this case refers to the displacement of the cantilever.

$$DFL = (A + B) - (C + D) \tag{2.1}$$

where DFL represents the sum of the deflection intensity and A, B, C and D represent the detected laser beam intensity in each quadrant [51]. The cantilever/tip is kept in close proximity with the sample by responding to the DFL value. The sensitivity of the feedback loop is set by the user such that the z axis controller is able to accurately maintain the tip-sample height by repositioning the tip. This general setup describes the majority of AFM experiments with specific adjustments made for more specialized methods. Of the many variants, tapping mode or amplitude modulated AFM (AM-AFM) and Kelvin Probe Force Microscopy (KPFM) will be discussed in more detail in this chapter.

2.1.1 Principles of Tapping Mode AFM

Tapping mode AFM, or amplitude modulated AFM is a type of AFM imaging that differs from a standard AFM measurement made in contact with the surface as described in the previous section as the tip-sample interaction is diminished due to the cantilever tapping the tip on the surface [53]. Specifically, the tip is driven at near resonant frequencies (typically offset by 5% in either direction of the resonant peak of the tip) which results in the tip effectively tapping on the surface. The instrument

is able to detect the change in tip frequency due to damping from tip-surface interactions. As in the standard contact AFM methodology, the piezoelectric actuator repositions the tip to the specified distance near the surface to recover the set drive amplitude [53].

The dominant contributions to the motion of the cantilever has been described [54] as the elastic response, tip-sample interaction, and its excitation force. This results [54] in the following nonlinear, second-order differential equation:

$$m\frac{dz^2}{d^2t} = -k_c z - \frac{m\omega_0}{Q} + F_{t,s} + F_0 \cos\omega t \tag{2.2}$$

where F_0 represents the amplitude of the tip, $F_{t,s}$ is the tip-sample interactions and ω the angular frequency of the tip driving force. Q, ω_0 and k_c are the quality factor, angular resonance frequency and the spring constant of the free cantilever.

The tip-sample interaction force ($F_{t,s}$) has been modeled with a sphere acting as the tip and a flat surface which has been demonstrated to be a reasonable approximation [54]. Eqn 2.3 demonstrates this tip-sample interaction:

$$F_{t,s}(z_c, z) = -\frac{Hr}{6(z_c + z)^2} \tag{2.3}$$

where H is the Hamaker constant, r is the tip radius, z_c is the sum of the tip-sample resting position and the distance between the sample and the tip itself; z is the instantaneous tip position.

Figure 2.3 illustrates how z_c and z are measured. z is measured from the tip's resting point when not oscillating to its minimum amplitude when oscillating. The distance between the sample and this minimum position is denoted as d ($d = z_c - z$) and z_c is ultimately the distance between the resting position of the cantilever and the sample itself.

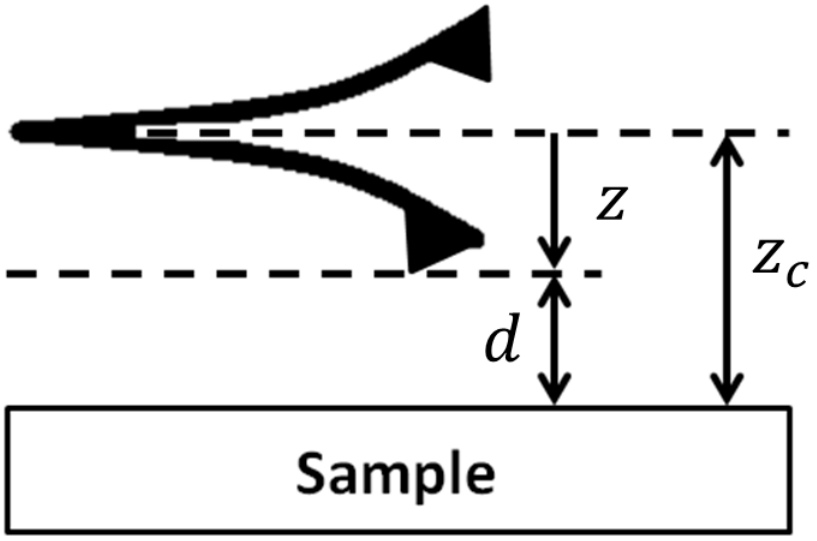

Figure 2.3: Position of AFM tip resting position and tip-sample distance. Adapted from [54]

The advantages of tapping mode AFM over other morphological mapping modes is that this tapping results in a more accurate map of the surface as it accounts for some tip-sample artifacts [55]. Tip dragging for example is reduced due to the fact that the tip is no longer in constant contact with the surface which in turn reduces the frictional forces acting on the tip from the surface. Furthermore, tip flexion is similarly reduced due to this diminished direct contact with the surface. This method of measurement is significantly less harsh on the tip, resulting in longer lasting tips for repeat measurements. As a consequence of this diminished contact with the surface the tip is also less prone to contamination from the surface itself and subsequently the tip is less prone to deformation/change from the surface itself. The issue of contamination is critical to other methods of AFM measurements, specifically KPFM.

2.2 Kelvin Probe Force Microscopy

Kelvin Probe Force Microscopy (KPFM) is an advanced AFM technique which allows for the precise mapping of both the morphological information of the substrate along with the generation of a work function map [56]. The work function is defined as the minimum amount of energy required to release an electron from a solid surface to vacuum [57]. This technique is particularly powerful as these measurements are performed consecutively allowing for direct mapping of the electronic properties of the surface to the morphological properties. KPFM measurements of surfaces occur in a dual pass fashion where the tip scans across the surface making a height measurement and on the second pass work function information is collected [56]. As this measurement occurs in tandem, this allows for correlation of the electronic properties to the morphological features of the surface.

The KPFM probing tip and the metallic substrate behave as a parallel plate capacitor in which an electrostatic force [56] exists between them as per Eqn 2.4:

$$F = \frac{1}{2}\frac{dC}{dz}V^2 \tag{2.4}$$

where dC is the change in capacitance and dz is the change in tip-sample separation.V represents the voltage between the surface and the tip. Eqn 2.4 demonstrates the dependence of height on the electrostatic force measured during the Kelvin probe experiment. To ensure the reliability of the measured work function map, the measurement is always made at constant tip-sample separation which is maintained by re-tracing the obtained morphological map while measuring the work function.

2.2.1 Determining contact potential difference (CPD) between tip and sample

The determination of the absolute work function of the sample is made possible due to this electrostatic force which exists between tip and sample as described in section 2.2 as Eqn 2.4 [58]. During the KPFM measurement, DC and AC voltages are applied. These voltages are described in Eqn 2.5:

$$V = (V_{DC} - V_{CPD}) + V_{AC} \cdot \sin \omega t \tag{2.5}$$

where V_{CPD} is the contact potential difference, V_{DC} is an applied bias and V_{AC} is the applied AC voltage which is applied near the resonant frequency of the tip, ω. Eqns 2.4 and 2.5 can be combined together to result in an overall expression for the net force [58]:

$$F = F_{DC} + F_{\omega} + F_{2\omega}. \tag{2.6}$$

Ultimately, the only force being considered during a KPFM measurement is the F_{ω} term. This is due to the system being tuned to the near resonant frequency of the tip which means only that force is being detected during this scan. The F_{ω} term can be expanded to the following:

$$F_{\omega} = \frac{dC}{dz}[V_{DC} - V_{CPD}]V_{AC} \cdot \sin \omega t. \tag{2.7}$$

Eqn 2.7 shows that the only variable term is V_{DC} which is the nulling bias designed to cancel out the V_{CPD} term and ultimately canceling the electrostatic force between tip and sample. This allows for the measurement of V_{CPD} which is known as the contact potential difference. This V_{CPD} term is the difference in work functions between the

tip and the sample and has the following form:

$$eV_{CPD} = \phi_{tip} - \phi_{sample} \tag{2.8}$$

where e represents elementary charge and ϕ_{tip} and ϕ_{sample} represent the work functions of the tip and the sample, respectively. This is shown schematically by Figure 2.4 which shows an energy level diagram with a tip and the surface represented.

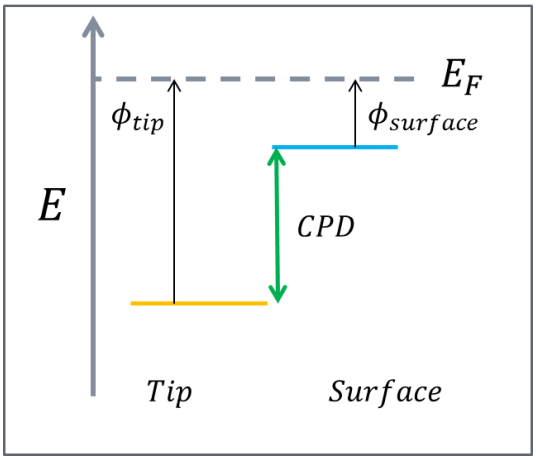

Figure 2.4: Energy level diagram of Pt, Au, and Cr work functions

Figure 2.4 demonstrates how CPD is calculated as the difference between work functions. Ultimately, the KPFM technique is rather powerful in that it is possible to directly map the electronic properties of a substrate to the morphological properties.

2.2.2 Metallic surface measurements with KPFM

Very little work has been performed which directly measures SERS substrates using KPFM [59], although there is still work being performed with KPFM for metallic surfaces. A search of the CAPLUS database shows that 1311 papers have been published since 2000 and that research employing this technique is growing as groups continue to implement KPFM measurements in to their studies. Figure 2.5 summarizes the

amount of publications on this topic since 2000.

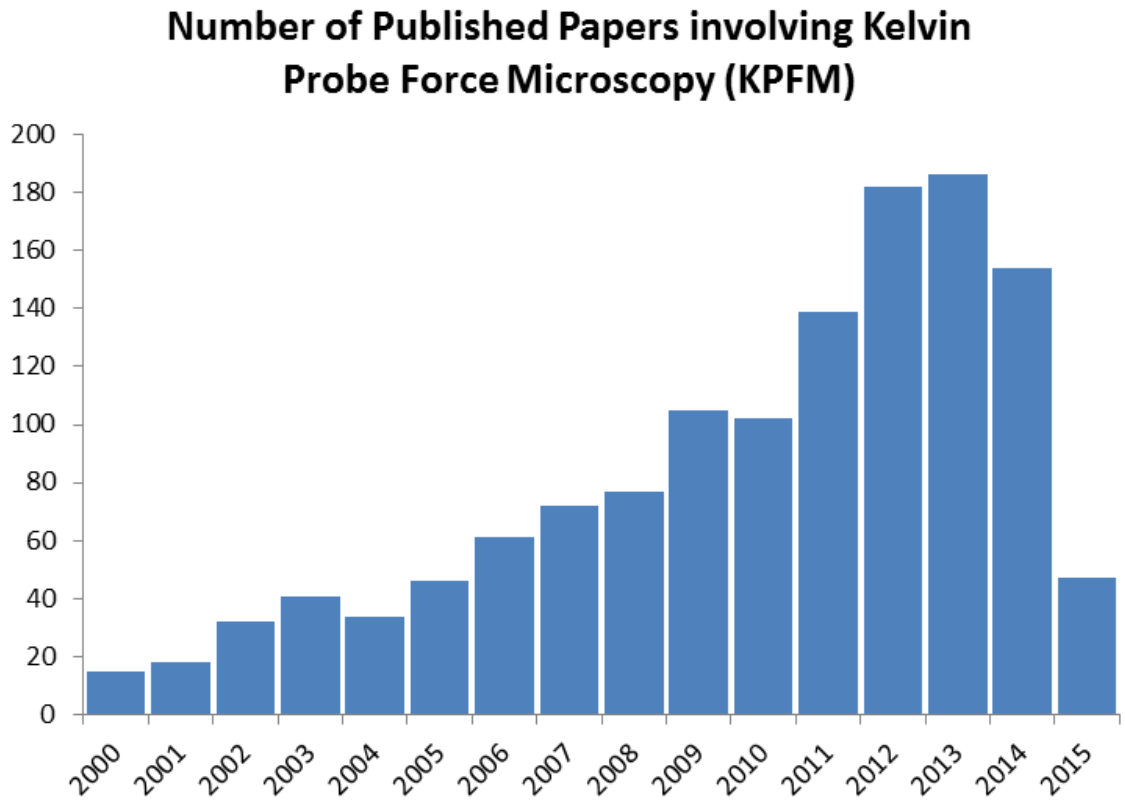

Figure 2.5: Publications by year on Kelvin Probe Force Microscopy (KPFM) (CAPLUS database, obtained on 5/3/2015)

Figure 2.5 shows that the use of KPFM has continued to grow since the turn of the millennium. Mapping the electronic and morphological properties of metallic surfaces is critical for understanding a wide variety of issues such as corrosion, solar cell design and charge transfer behavior. Recent advances in the field will be discussed and how KPFM has been employed to facilitate these studies.

2.2.2.1 Corrosion studies *via* KPFM

Corrosion specifically refers to the chemical and biological processes which contribute to the removal and destruction of a material. When designing materials there is a significant need to understand its macro scale properties by investigating its micro

and nano scale properties which is where KPFM proves to be an excellent surface analysis technique. Understanding the electronic properties that give rise to these particular issues is paramount to developing robust and efficient materials. In recent years, groups such as de Wit's [60–62], Pan's [63, 64] and Andreatta's [65, 66] have been actively tackling the specific issue of corrosion in metallic systems. The research performed by de Wit's group in particular focuses on the corrosion behavior of various metallic alloys by specifically investigating how the workfunction changes through various treatments. In one particular study [60] Al brazing sheets were studied by observing how heat treatments affected the contact potential difference and subsequent corrosion of the material. Figure 2.6 demonstrates the results of their measurements from various line profile measurements across the Al brazing sheet surface and determining the CPD (referred to as Volta potential difference in this paper) of the brazed and non-brazed surfaces.

Their findings indicated that there was a significant increase in CPD with brazing which in turn reduces the corrosion protective abilities of the cooled brazing sheet [60]. This overall increase in CPD ultimately corresponds to a decrease in robustness in terms of the brazing material and its re usability. This is merely one specific example of how KPFM has been used to assess corrosion directly, however this technique is routinely used when determining the effectiveness of anti-corrosion coatings [66].

2.2.2.2 Photovoltaic cell design and charge transfer studies

Photovoltaic cells (solar cells) design is an absolutely massive field of research in science given demands for cheaper and more efficient energy sources. Many groups have been actively researching methods for reducing materials costs, such as employing thin films to reduce the quantity of bulk material used [67]. Groups such as Palermo's [68–70], Sadewasser's [71,72] and Takahashi's [73–75] have been actively characterizing

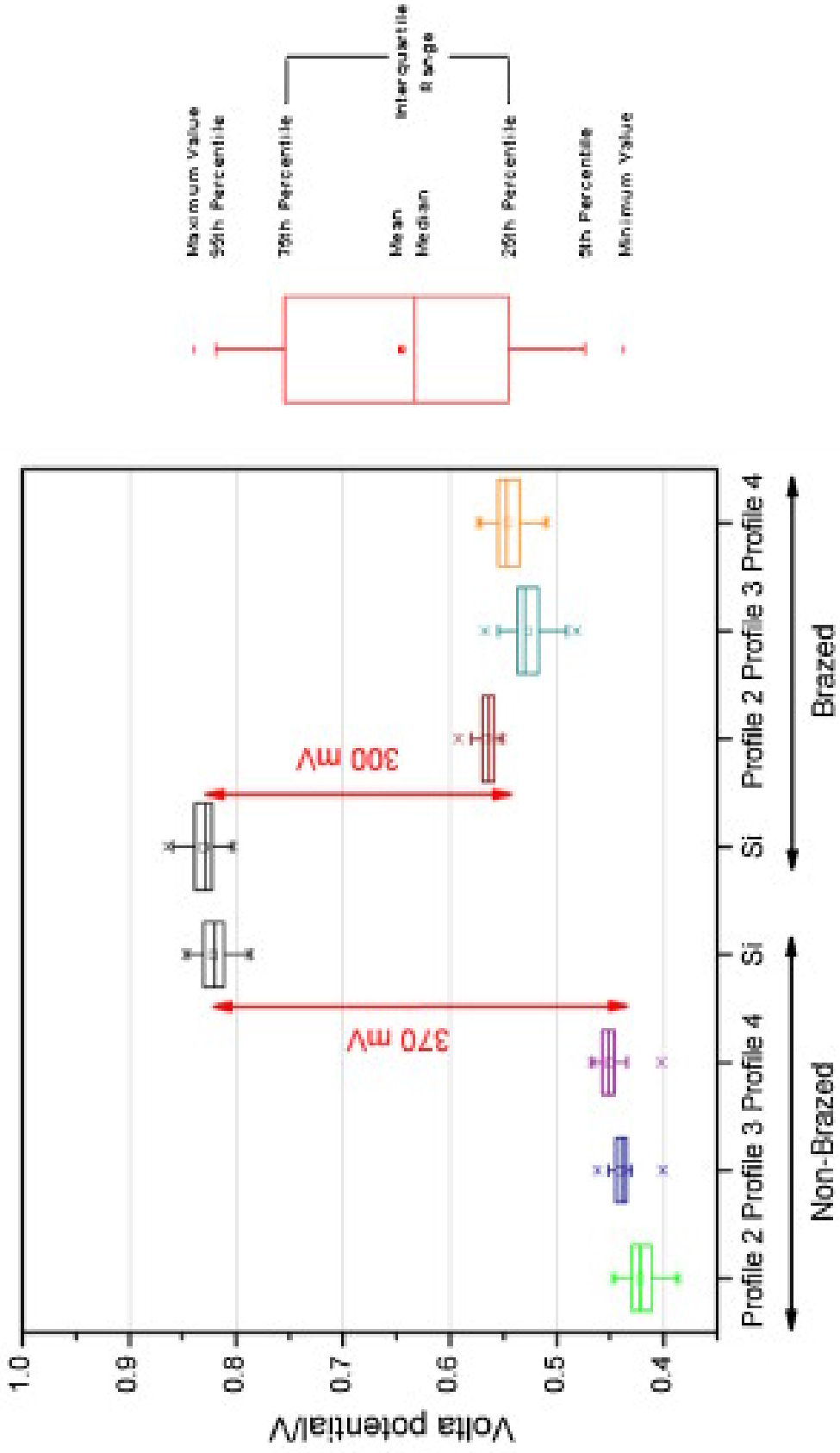

Figure 2.6: Box chart representation of the CPD profiles from cross sectional analysis of Al brazing sheets. Reprinted from Electrochimica Acta. 104, F. Norouzi Afshar, A.M. Glenn, J.H.W. de Wit, H. Terryn, J.M.C. Mol [60], A combined electron probe micro analysis and scanning Kelvin probe force microscopy study of a modified AA4xxx/AA3xxx aluminium brazing sheet, 58, 2013, with permission from Elsevier.

these newly developed thin film structures with Kelvin probe force microscopy. One technique in particular that they take advantage of is called photo-KPFM which follows the same principles of normal KPFM however the measurement is made prior to irradiation and then subsequently remeasuring the substrate during irradiation at a selected wavelength. For a detailed schematic of this method, refer to chapter 3.2.2.3 of this thesis where this technique is described and employed.

As previously mentioned, no direct photo-KPFM measurements of SERS substrates have been performed but photo-KPFM usage outside of this specific application is being used often as previously mentioned. Palermo and his colleagues study thin film depositions of photovoltaic blends and monitor the charge transfer *via* photo-KPFM. In one particular study [68] organic electron donor and acceptor compounds were blended together and formed into films through a selective solvent vapour annealing process. These produced films were then analyzed *via* KPFM with and without white light irradiation. The subsequent changes in the workfunction of the various surface features were then analyzed to determine how the charge transfer between the "blended" materials was affected. Figure 2.7 summarizes their results.

As is demonstrated in Figure 2.7, it was found that there was a significant increase in measured potential post illumination on the features identified on the surface morphology. As per their cartoon schematic, it is noted that the photoactive regions are only observed when both the electron acceptor and donor were in direct contact with each other. From this, it was observed that when this contact was formed, the surface potential increased significantly when irradiated as d and h indicate in Figure 2.7. The authors attribute this increase in potential contrast to zones where exciton splitting and charge generation occurs which is at the direct acceptor-donor junction.

The ability to map the morphological and electronic properties of the surface with and without excitation is incredibly useful for determining how the electronic prop-

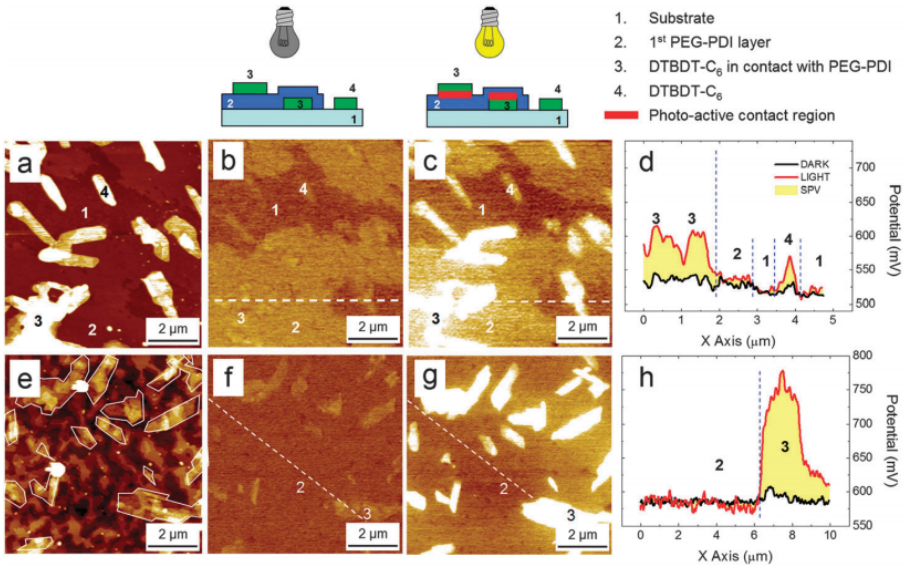

Figure 2.7: Topographical (a,e) and corresponding non-irradiated (b,f) and irradiated (c,g) electronic maps as measured by KPFM of photovoltaic blended thin films and their corresponding line trace profiles (d,h). Reproduced from [68] with permission of The Royal Society of Chemistry.

erties of surfaces are directly affected by light absorption. Work using this technique serves as a direct motivation for the research presented in this thesis and this technique is directly employed to help elucidate the physical and electronic properties of SERS substrates during and in the absence of direct illumination.

Chapter 3

Investigation of novel Au-Cr nanostructured substrates

3.1 Motivation

Marine contamination as a result of the oil extraction process is a constant source of concern for both the general public and the oil and gas industry [76]. During the production process, sea water is pumped down into the well so as to force oil to the surface. This contaminated water is referred to as produced water (PW). Produced water is released back into the environment following treatment during the oil extraction process and is known to contain a wide variety of polycyclic aromatic hydrocarbons (PAH's) [77]. PAH's as a class of compounds are well understood to have adverse health effects [78] and proper monitoring of these compounds is of crucial importance.

This study focuses on phenanthrene as a target molecule using SERS as the detection method. SERS is a technique which takes advantage of the optical properties of metal substrates to greatly increase the intensities of adsorbed analytes vibrational

modes [22]. This allows for great specificity due to the unique nature of the pattern of vibrational modes observed during a Raman measurement. Secondly, this is beneficial in lieu of IR spectroscopy as the measurements are made in water. Water containing IR spectra are typically of little use due to the large vibrational modes observed at higher wavenumbers. For further background information on Raman and SERS, refer to section 1.1 of this thesis. This behavior is not observed in Raman measurements. [1] Finally, due to the relatively low concentrations expected (approximately 0.3 ppb [79]) the significant intensities observed during SERS makes it the ideal detection method for oil-in-water samples. This project uses photo-KPFM to compare morphological, electronic, and optical properties of the substrates and compared them to the observed enhancement factors from the SERS measurements. One of the key advantages of employing SPM for these morphological measurements is the capability for sub-Ångstrom resolution in the height determinations. The goal of these measurements is to guide future sensor designs in determining which properties correlate with one another.

3.2 Experimental procedure

3.2.1 Au-Cr nanostructure preparation

The preparation of Au-Cr nanostructured films is based on a procedure previously described in B. Moazzez's doctoral thesis [80]. Microscope glass slides (Cole-Parmer precleaned 25 × 75 × 1.00 mm plain) were cut into three equivalent pieces using a diamond scribe (SPI supplies) and then were rinsed with 95% EtOH, 30% acetic acid and finally nanopure water (Barnstead, 18.2 MΩ·cm.) The glass surfaces were then dried using filtered, dried compressed air. The metal evaporation occured in an in-house built metal evaporation system under high vacuum. The glass slides

were placed in a circular sample holder disc which was mounted 20 cm above the metal evaporation source and level with a quartz crystal microbalance (QCM) to monitor metal deposition thicknesses (INFICON XTM/2 depositon monitor.) Gold wire (Alfa Aesar, 99.9% metal basis purity) was placed in a tungsten wire basket and chromium pellets (Alfa Aesar, 99.5%) were placed in a separate tungsten boat within the evaporation chamber. The evaporation chamber was fitted with a glass bell with a protective exterior cage prior to evaporation. Metal deposition was performed at pressures below 10^{-8} Pa by evaporating Cr to a thickness of 17 nm as per QCM measurements and then switching to evaporation of Au to a thickness of 27 nm. This switching occurred by placing an internal shutter over the Cr source and by applying voltage to the Au source, thus starting the Au evaporation. This results in Cr as a base layer with Au forming the top layer. These subsequent evaporations were performed without exposing the vacuum chamber to ambient air so as to limit any potential Cr oxidation during evaporation. The system was allowed to cool to room temperature prior to exposing the chamber to atmosphere.

The bimetallic films were then placed in a programmable furnace and annealed for 2 h at either 300, 350, 400, or 450 °C. One set of bimetallic films was left unannealed so as to compare with the annealed samples. All samples were prepared in duplicate such that one set of samples was viable for SERS measurements and the other set was used for UV-Vis and photo-KPFM measurements.

3.2.2 Characterization Techniques

3.2.2.1 UV-Vis spectroscopy

The plasmonic absorptions of the films were measured using a USB2000 (Ocean Optics) UV-Vis spectrophotometer with R200 reflection split fiber probe arranged in a

planar transmission geometry relative to the films. Samples were measured from 290 to 890 nm with an acquisition time of 10 ms. A glass slide washed as per the steps listed in section 3.2.1 was used as a light reference for UV-Vis measurements.

3.2.2.2 SERS studies

Raman spectra were acquired after submerging the samples in 1.6 ppm phenanthrene (aq) (>98%, Sigma Aldrich) for 30 min. The samples were then removed, rinsed with nanopure water (Barnstead, 18.2 M Ω·cm) and then allowed to air dry for 30 min. The spectra were collected with an inVia Raman microscope (Renishaw) equipped with an 830 nm laser source with 3.0 ± 0.3 mW power, under 20x magnification with a 30 s exposure time. Unexposed sample Raman spectra are compared with exposed samples to determine the presence of adsorbed phenanthrene. Resultant exposed Raman spectra were also compared with the spectra of bulk phenanthrene to determine peak assignments. All spectra were acquired in triplicate for statistical analysis. For the enhancement factor calculations, measurements were made using an ethanolic solution of 0.1 ppm phenanthrene to compare.

3.2.2.3 Photo-KPFM analysis

KPFM images were acquired using a MFP-3D (Asylum Research) in scanning Kelvin probe microscopy (SKPM) mode. The substrates were measured using a conductive Pt/Ti tip (Mikromasch, NSC35) with a nominal frequency of 145 kHz. All measurements were made at room temperature and atmospheric pressure. The samples were placed on the ORCA (Asylum Research) sample holder with a Au clip connecting to the sample. A wire lead from the cantilever holder connects with a gold pad connecting to the sample, as per Figure 3.1.

All acquired images were 5 μm x 5 μm with 256 points per line, collected at a

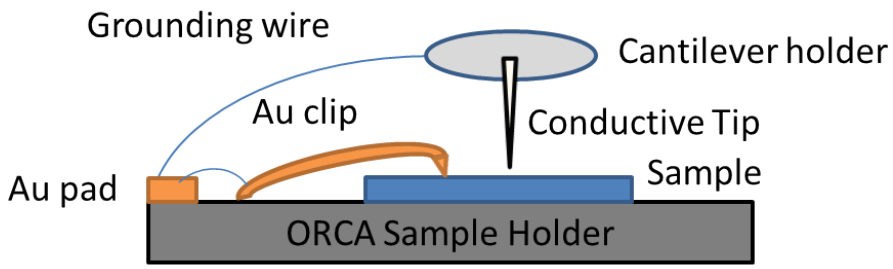

Figure 3.1: Schematic diagram of ORCA sample holder used for KPFM setup

rate of 0.5 Hz. For the KPFM scans, samples were measured at 5 nm tip-sample separation during the second pass with a tip with a work function of 4.914 eV. Tip calibration was performed by first measuring freshly cleaved HOPG which has a known work function of 4.6 eV [81]. Photo-KPFM imagery was collected by consecutively measuring the substrates *via* KPFM with and without illumination. For the photo-KPFM pass, the images were illuminated by a broad wavelength lamp arranged at 90° relative to the sample stage at a distance of 0.3 m. No image processing was applied to the KPFM imagery; a first order flatten was applied so as to level the height maps of the substrates. The software first sets the average value of each scan line to zero, followed by the first-order flatten procedure which removes the "tilt" in an image by subtracting a linear function from each scan line. Statistical measurements were made by dividing the resultant micrograph into four equivalent quadrants of 2.5 μm^2 area. Image analysis was performed using AR130370 (Asylum Research, Oxford Instruments.) For grain size calculations Gwyddion [82] was employed.

3.3 Results and Discussion

3.3.1 Plasmon band determination

UV-Vis spectroscopy was performed to determine the position of the samples' plasmon bands and to determine how annealing affects the absorption wavelength. For SERS substrates it is important that the sample is able to absorb at the laser wavelength [83], which in this case was 830 nm. When the sample absorbs at the laser wavelength, surface plasmons will be excited which in turn results in a greater electric field. This newly generated electric field is critical for SERS as it directly promotes the SERS effect. Figure 3.2 shows the results of this experiment.

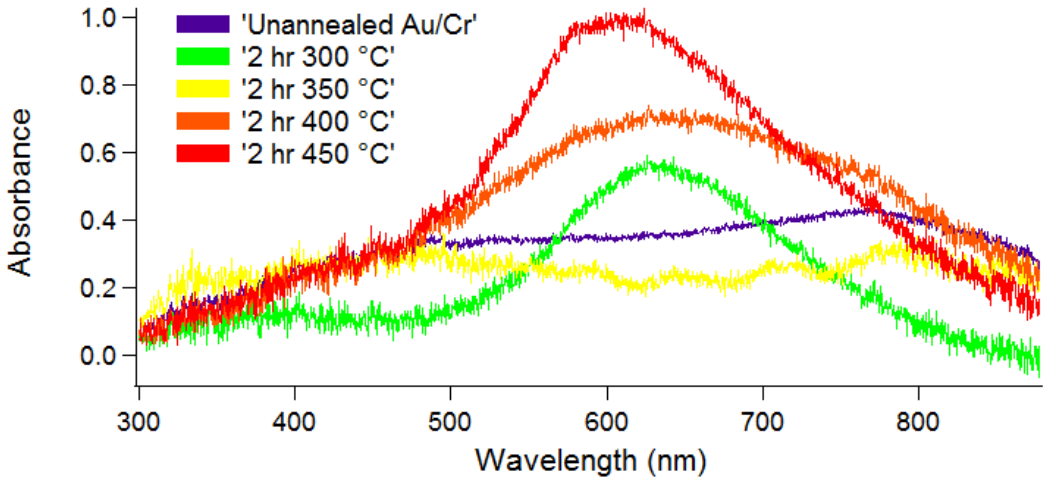

Figure 3.2: Collected absorption spectra of unannealed and annealed Au/Cr SERS substrates

It is noted that as the annealing temperature increases, λ_{max} shifts to higher energy absorption maxima. Furthermore, all samples were shown to have some absorbance at 830 nm which was promising for potential viability as SERS substrates with the 830 nm laser source employed. The absorption at 830 nm (A_{830}) is tabulated in Table 3.1.

Table 3.1: Summary of absorbance at $\lambda = 830nm$ for prepared Au/Cr substrates

Sample	A_{830}
Unannealed	0.362
300 °C	0.062
350 °C	0.280
400 °C	0.362
450 °C	0.280

3.3.2 Morphology of substrates

Surface morphology information was collected during the KPFM measurements of the Au/Cr substrates. Of these, three key properties were investigated: root-mean-square roughness (R_{RMS}), surface area (SA), and grain size. Roughness was calculated *via* the root-mean-square method [84] with Eqn 3.1:

$$R_{RMS} = \sqrt{\frac{1}{n}\sum_{i=1}^{n} z_i^2} \tag{3.1}$$

where z represents the height deviation from the mean plane within the sample area for all n given points. The surface area was calculated by applying a quaternary triangular mesh (QTM) to the surface and calculating the surface area of the resultant triangles across the surface [84]. Grain size was determined by using the Vincent segmentation method [85]. The resultant height images are depicted in Figure 3.3. A summary of all morphological parameters investigated is presented in Table 3.2.

Annealing temperature and roughness show results consistent results described by De Los Santos [86] and are shown in Figure 3.4. It is observed that as annealing temperature increases, surface roughness remains constant until 350 °C where a significant drop occurs. At this point roughness reaches a minimum value before increasing dramatically due to grain coarsening as roughness increases to 450 °C. This grain

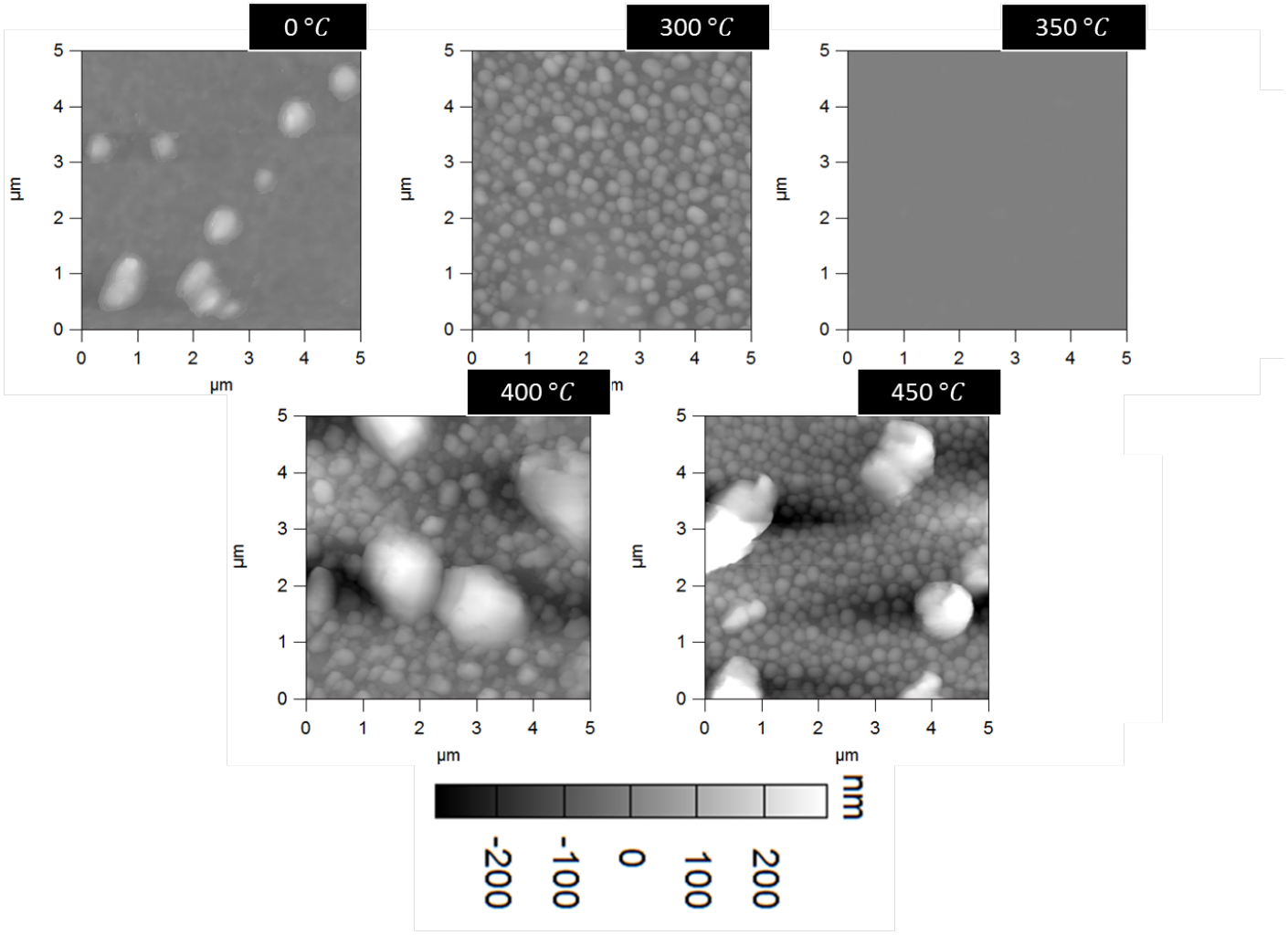

Figure 3.3: Height maps of all Au/Cr substrates. All images use the same z colour scale

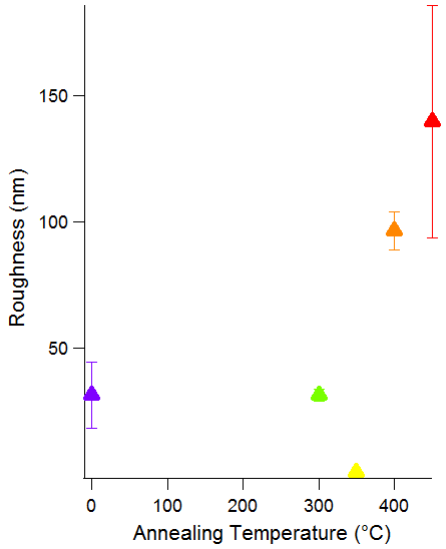

Figure 3.4: Effect of annealing temperature on roughness of Au/Cr nanostructured substrates

Table 3.2: Morphological properties obtained through KPFM analysis

Sample	R_{RMS} (nm)	SA ($nm^2 \times 10^5$)	Grain size (nm)
Unannealed	31.15 ± 13.39	71.0 ± 5.9	87 ± 33
300 °C	31.10 ± 2.31	75.0 ± 2.0	170 ± 20
350 °C	0.70 ± 0.07	62.3 ± 0.5	139 ± 1
400 °C	96.23 ± 7.64	7.3 ± 1.0	303 ± 78
450 °C	139.6 ± 46.0	85.0 ± 2.8	146 ± 62

coarsening is quite apparent in the AFM micrographs presented in Figure 3.3. The non linear dependence of temperature on Au roughness values has been previously studied [86] and our results are consistent with prior findings with a roughness minimum observed at 350 °C and subsequently increases at higher temperatures. From literature it is noted that Au typically dewets at 300 °C and aggregates into larger Au islands with increased temperature [87, 88] This increase in roughness is promising as literature has shown a clear relationship between roughness and SERS activity [89], due to changing plasmonic behavior of the substrate.

3.3.3 SERS Trials

All exposed substrates demonstrated SERS activity. This was determined by comparing the resultant spectra with the non-exposed substrate and bulk phenanthrene. As seen in Figure 3.5 there are a significant amount of common peaks in both the SERS spectrum and the normal Raman spectrum of phenanthrene. These overlapping peaks between both spectra exemplify the detection of phenanthrene using our Au/Cr substrates. It is noted that for the purposes of clarity, the bulk phenanthrene has had its intensity scaled by a factor of 10 so as to compare peak positions between the bulk phenanthrene and the exposed Au/Cr substrates. This was necessary due to the significant enhancement produced by these Au/Cr substrates.

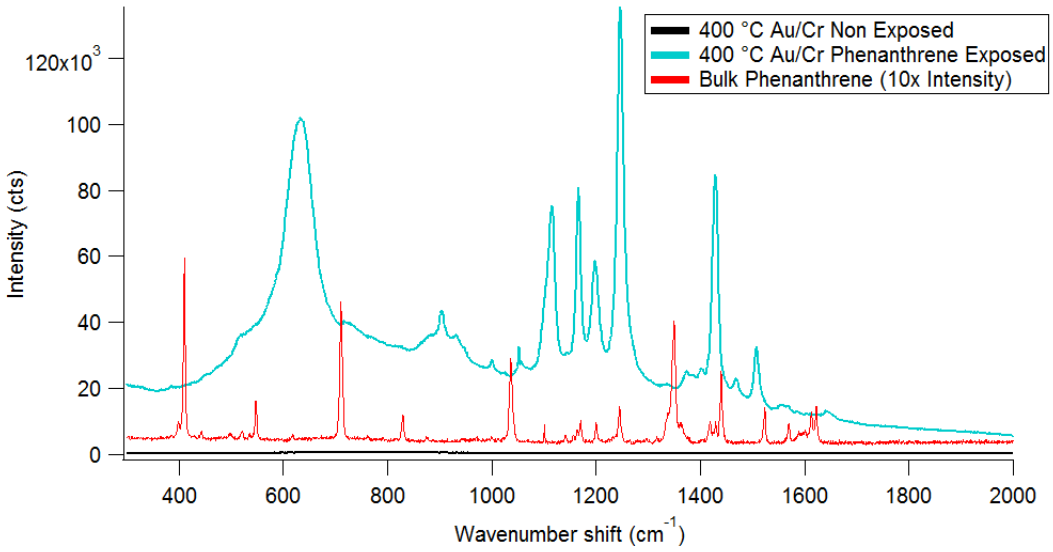

Figure 3.5: Demonstration of SERS activity comparing the Raman spectrum of bulk phenanthrene (Scaled to 10x intensity for clarity) to that of the phenanthrene-exposed annealed substrate

To show that the enhanced signal was driven specifically by the prepared substrates and not a general surface adsorption phenomenon, the spectra of both phenanthrene-exposed and non-exposed bare glass are shown as well (Figure 3.6). The non exposed and exposed glass substrates show identical spectra with a large fluorescence band

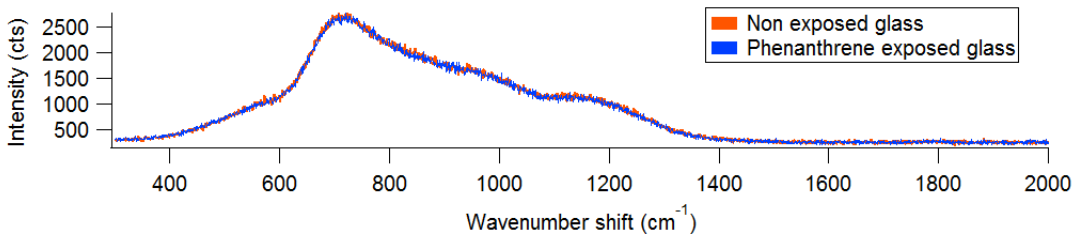

Figure 3.6: Comparison of exposed and non-exposed glass substrate

beginning at 400 cm^{-1} and going to 1400 cm^{-1}. As there are no observable peaks beyond 1400 cm^{-1} this suggests that phenanthrene was not adsorbed to the surface of the glass and that any phenanthrene signal observed with the tested Au/Cr substrates was due to adsorption of phenanthrene to the SERS substrate specifically.

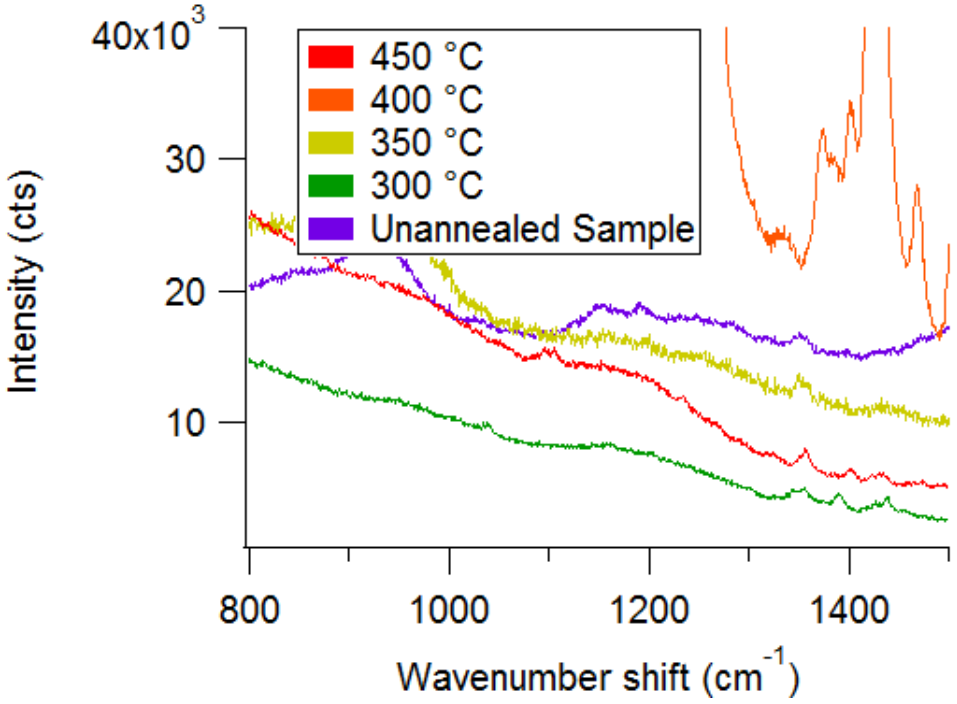

Figure 3.7: Phenanthrene exposed Au/Cr substrates' common peak near 1350 cm^{-1}. Peaks have been shifted for clarity.

All exposed Au/Cr samples demonstrated SERS activity with a common peak observed between all samples near 1350 cm^{-1} which corresponds to a mode of C-C

stretching and H-C-C stretching in phenanthrene [48]. Figure 3.7 shows the common peak near 1350 cm^{-1} for all Au/Cr substrates. Relatively small shifts in this peak can be attributed to the nature of the analyte adsorption to the surface. As this peak was common to all exposed substrates, this peak was employed to perform the enhancement factor (EF) calculations as per Eqn 3.2 [90]:

$$EF = \frac{I_{SERS}}{I_{normal}} \times \frac{C_{normal}}{C_{SERS}}. \tag{3.2}$$

I_{SERS} was determined by measuring the peak height near 1350 cm^{-1} for each respective substrate, and I_{normal} was measured similarly using a 0.1 ppm ethanolic solution of phenanthrene. Using surface area (SA) measurements obtained from KPFM, it was possible to correct for geometry in Eqn 3.2 to result in a new property, the surface area scaled enhancement factor (EF^*). This has the following form:

$$EF^* = \frac{EF}{SA}. \tag{3.3}$$

This geometric correction is useful as it accounts for any potential concentration effects of the adsorbed phenanthrene on the substrate contributing to an increase in the overall enhancement factor therefore resulting in a more accurate calculation of enhancement factor. A summary of these results are presented in Table 3.3.

Table 3.3: Enhancement Factors of Au/Cr samples

Sample	$EF \times 10^5$	$EF^* \times 10^{-2}$ (nm^{-2})
Unannealed	1.260 ± 0.244	1.788 ± 0.377
300 °C	1.470 ± 0.074	1.960 ± 0.111
350 °C	0.424 ± 0.099	0.682 ± 0.159
400 °C	0.495 ± 0.161	0.671 ± 0.218
450 °C	1.335 ± 0.243	1.571 ± 0.291

3.3.4 Electronic properties of substrates

KPFM measurements were performed on the Au/Cr substrates under broad wavelength illumination and without. In all cases, it was noted that the subsequent photo work function map was on average always lower than the standard work function map. This data has been summarized in Table 3.4, with $p\phi$ representing photo-work function and normal work function as ϕ.

Table 3.4: Electronic properties of Au/Cr substrates

Sample	$\phi(eV)$	$p\phi(eV)$
Unannealed	4.396 ± 0.011	4.788 ± 0.035
300 °C	4.769 ± 0.071	4.774 ± 0.068
350 °C	5.094 ± 0.005	5.099 ± 0.006
400 °C	4.322 ± 0.074	4.371 ± 0.073
450 °C	4.466 ± 0.097	4.587 ± 0.091

3.4 Interaction between electronic properties and SERS activity

All Au/Cr substrates showed SERS activity, but there is quite a range of enhancement among the different annealing temperatures. The morphology or absorption spectra alone cannot explain the variance between samples, as seen in Figures 3.8 and 3.9. The electronic properties of the substrates revealed some evidence towards the variability between samples, however showing direct correlation between the normal work function and EF* was not observed as observed in Figure 3.10.

To better represent the experimental conditions during SERS trials, photo-work function measurements using broad wavelength were employed, which showed a narrower work function range at which EF* is at its maximum. These values, along with

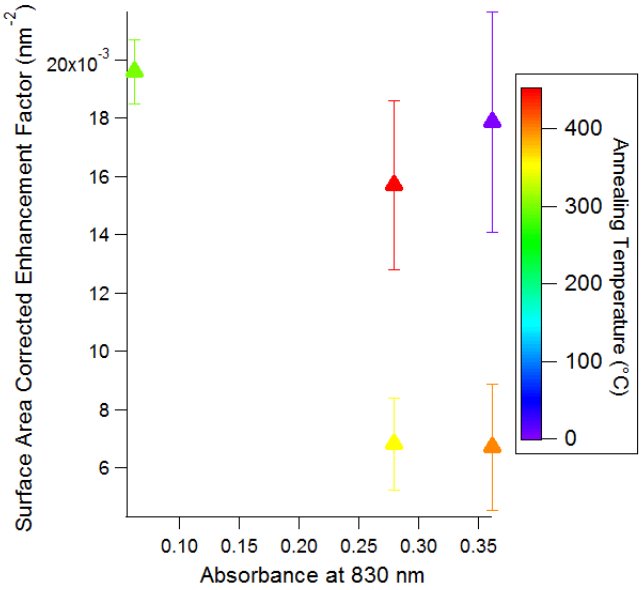

Figure 3.8: Plot of EF* and the absorption maxima at 830 nm showing no relationship

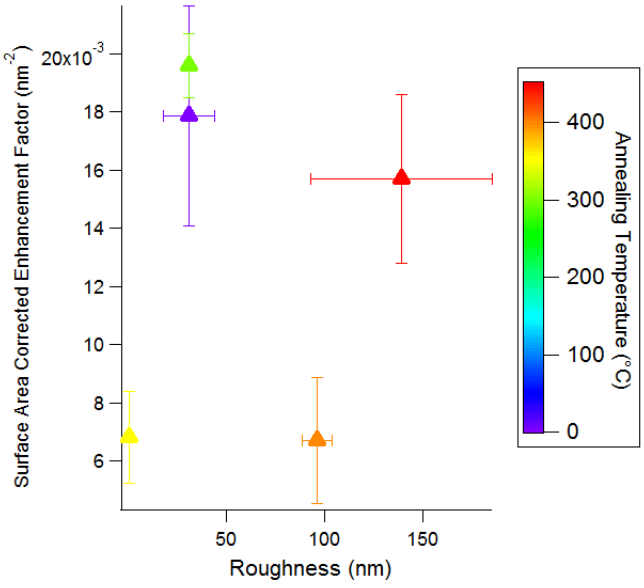

Figure 3.9: Plot of EF* and surface roughness showing no clear relationship

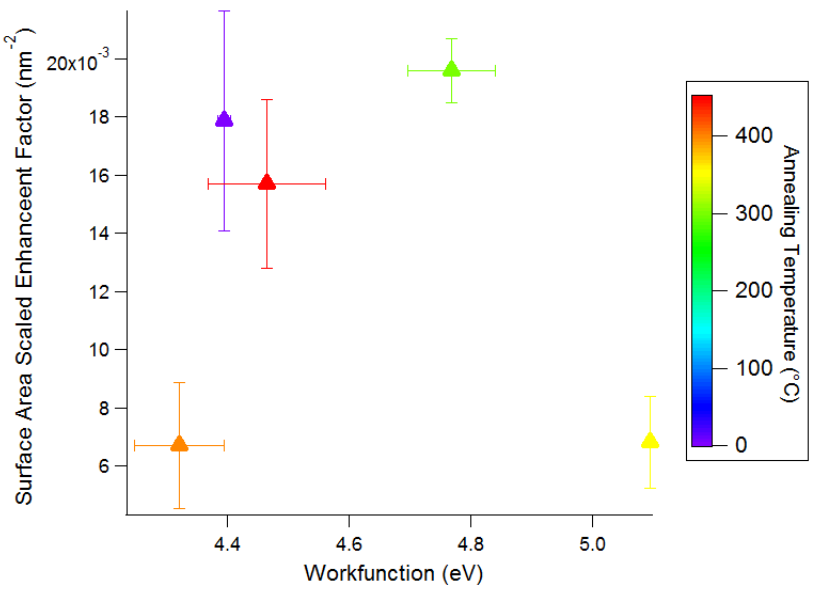

Figure 3.10: Relationship between EF* and ϕ demonstrating the optimal range for increased SERS intensity

literature values for phenanthrene's calculated [91] and experimental [92] HOMO-LUMO energy gap have been presented in Figure 3.11.

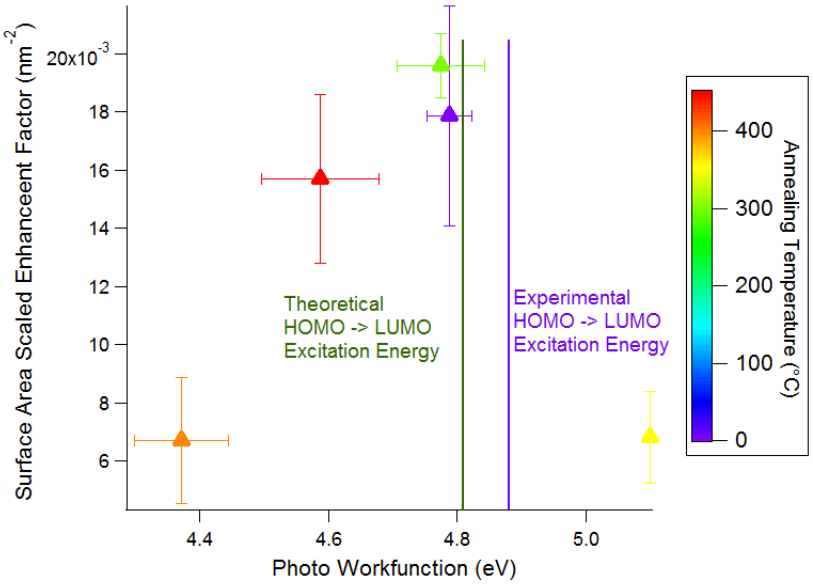

Figure 3.11: Relationship between EF* and $p\phi$ demonstrating a narrow optimal range approaching towards literature HOMO-LUMO gap energies corresponding to increased SERS intensity

From Figure 3.11, it is observed that as the $p\phi$ of the substrate approaches the HOMO-LUMO gap energy of phenanthrene, an increase in EF* is observed. This increase in intensity appears to occur due to energy matching between the substrates' $p\phi$ and phenanthrene itself. From this experiment, it is suggested that when phenanthrene and the substrate have an energy "match" there is a significant increase in intensity. Conversely, the substrates which have disparate photo work functions have lower overall SERS intensities. It is worth noting here that this is not merely a concentration effect on the surface as the EF has been scaled with respect to surface area and should correct for this effect.

These results indicate an optimal work function range required for maximizing the SERS response of phenanthrene; a potentially key design screening mechanism for future SERS substrate development. Further experimentation is absolutely required to determine the validity of the proposed substrate-analyte energy match model. Specifically, it is important to investigate other analytes with similar properties as phenanthrene and determine if this energy matching occurs with other SERS active substrates. Similarly, a technique such as DESI-MS (Desorption Electrospray Ionization-Mass Spectrometry) [93] should be performed on all substrates to accurately correct for concentration effects on the surface to reliably determine the amount of adsorbed phenanthrene on the surface of the substrates. Furthermore, it would be beneficial to validate these experiments with replication of the photo-KPFM study using 830 nm illumination as opposed to the broad wavelength lamp employed during this study.

3.5 Conclusion

Au/Cr thermally annealed systems demonstrate clear SERS activity with 830 nm excitation. The AFM studies show how the morphology of the substrates can be controlled *via* specific heating profiles shown in this thesis. Roughness, surface area, and grain size can be modified through this method resulting in nanostructured Au/Cr films. Similarly, the absorption properties of these substrates are directly influenced by the formation of the nanostructured films as evidenced by UV-Vis spectroscopy. It is clear that these nanostructured films give rise to significant SERS activity and allow for the detection of low concentrations of aqueous phenanthrene. The electrical properties of the substrates appear to play a key role in the intensity of the SERS response in that as the $p\phi$ of the substrate approaches the HOMO-LUMO energy of the target analyte, SERS response increases. This approach could be an effective screening mechanism for future SERS substrate development and provides a deeper understanding of SERS phenomena.

Chapter 4

Spheres Patterned SERS Substrates[1]

4.1 Motivation

The environmental effects of the oil extraction industry are well understood [76] and are a continual source of concern for the globe. During the production process, sea water is pumped down into the well so as to force oil to the surface. Water that is employed during oil production is treated and released back into the ocean once it is determined to be safe for the environment. Polycyclic aromatic hydrocarbons (PAHs) are a class of compounds which are known to be produced with oil recovery [77] with suspected adverse health effects [78]. This study uses phenanthrene as a target PAH analyte with detection using a class of novel SERS substrates. As the target analyte is aqueous phenanthrene, Raman spectroscopy was a natural fit for a number of reasons. Primarily, due to the relatively low concentrations (approx. 0.3 ppm) [79] measured, SERS is useful due to the significant intensities observed. Ultimately, this

[1]The author performed KPFM measurements and analysis on the provided samples. Sample preparation was performed by Dmytro Grebennikov and Abhijit Chatterjee.

powerful optical detection method allows for high specificity at low concentrations in an aqueous environment.

The purpose of this study was to explore the effect of the charge transfer mechanism using KPFM and SERS measurements. This was performed by employing bimetallic SERS substrates pre-patterned with SiO_2 spheres. This specific geometry was employed to tune the absorption of the substrates closer to 830 nm, the laser wavelength employed in this experiment. The charge transfer mechanism was specifically explored by adjusting the order of the bimetallic films deposited on the spheres substrates to see how the work function changes with respect to the order of the bimetallic films and by varying the thicknesses of the metals. For further information regarding the charge transfer mechanism, refer to section 1.2.2.2. Depending on the order and thickness of the metal layer(s) employed, there was a marked change on the resultant work function of the substrate and the results of these studies are presented in this chapter.

4.2 Experimental procedure

4.2.1 Sample preparation

Sample were prepared on glass microscope slides (Cole-Parmer precleaned 25 × 75 × 1.00 mm plain) which were cut into three pieces using a diamond scribe (SPI). These glass slides were then cleaned by first washing with concentrated H_2SO_4 and concentrated HCl and finally rinsed with nanopure water (Barnstead, 18.2 MΩ·cm.) Silica spheres with a diameter of 750 nm (Fiber Optics Center Inc.) were added to 2-butanone (Sigma Aldrich, 99%) to a concentration of 15% by mass. The spheres were then dispersed by sonication for 3 hr. This sphere suspension was then spin coated on to glass slides at 3000 rpm for 1 min, and then 495 poly(methyl methacrylate)

(PMMA) solution (Micro Chem) was spin coated on the sphere substrate at 1800 rpm or 2500 rpm for 1 min resulting in 75 nm and 66 nm [94] thick layers of PMMA, respectively.

The polymer spin coated substrates then had metals deposited on them *via* thermal evaporation under high vacuum in an in-house built metal evaporation system. The spin coated spheres samples were placed in a circular sample holder disc which was mounted 20 cm above the metal evaporation source and level with a quartz crystal microbalance (QCM) to monitor metal deposition thicknesses (INFICON XTM/2 depositon monitor.) Gold wire (Alfa Aesar, 99.9% metal basis purity) was placed in a tungsten wire basket and silver shot (Alfa Aesar, 99.9% metal basis purity) were placed in a separate tungsten boat within the evaporation chamber. The evaporation chamber was fitted with a glass bell with protective exterior cage prior to evaporation. Metal deposition was performed at pressures below 10^{-8} Pa to create a number of samples with varying top layer thicknesses.

One set of samples had 10 nm Ag evaporated first, followed by 15 or 25 nm Au on top. The other set had 10 nm Au as a base layer with 15 or 25 nm Ag as the top layer. Finally, a set of samples with 15, 25 and 35 nm of only Au was prepared. All sample evaporations occurred sequentially without exposing the system to atmospheric conditions so as to minimize potential Ag oxidation. This was achieved by first applying voltage across one metal source, engaging the internal shutter to terminate deposition when the desired thickness was achieved as per the QCM, and then switching the voltage to the other metal source and depositing to the desired thickness. Table 4.1 summarizes all prepared samples.

Table 4.1: Film thickness parameters of prepared samples. All films were deposited on a layer of 750 nm SiO_2 spheres.

PMMA (nm)	Bottom layer	Top layer
	(Metal, thickness)	(Metal, thickness)
75	–	Au, 15 nm
75	–	Au, 25 nm
75	–	Au, 35 nm
66	–	Au, 15 nm
66	–	Au, 25 nm
66	–	Au, 35 nm
66	Ag, 10 nm	Au, 15 nm
66	Ag, 10 nm	Au, 25 nm
66	Au, 10 nm	Ag, 15 nm
66	Au, 10 nm	Ag, 25 nm

4.2.2 KPFM analysis

KPFM images were acquired using a MFP-3D (Asylum Research) in SKPM [56] mode. The substrates were measured using a conductive Pt/Ti tip (Mikromasch, NSC35) with a nominal frequency of 145 kHz and a work function of 4.914 eV. Tip calibration was performed by first measuring freshly cleaved HOPG which has a known work function of 4.6 eV [81]. The samples were placed on the ORCA (Asylum Research) sample holder with an Au clip connecting to the sample. A wire lead from the cantilever holder connects with a gold pad connecting to the sample and all measurements were made at room temperature and atmospheric pressure. A detailed schematic of this experimental setup is available in Figure 3.1. All images included here were 5 μm x 5 μm with 256 lines and 256 points per line, collected at a rate of 0.5 Hz. For the KPFM imagery, samples were measured at 5 nm tip-sample separation during the second pass. No image processing was applied to the KPFM imagery; a first order flatten was applied to the height maps of the substrates. The procedure for the

determination of grain size and roughness has been summarized in Section 3.2.2.3 of this thesis.

4.3 Results and discussion

4.3.1 Au thin films morphological and electronic properties with 75 nm PMMA base layer

KPFM measurements were performed on all samples listed in Table 4.1 so as to determine their morphological and electronic properties. The purpose of these measurements was to provide mechanistic evidence of the role that variable thickness PMMA plays in terms of observed SERS activity. Figure 4.1 and Table 4.2 summarize the results obtained from 15, 25 and 35 nm thick Au films on 75 nm thick PMMA. For Figure 4.1 the z-axis represents work function. Brighter regions on the map indicate high work function; darker regions indicate low work function.

Table 4.2: Summary of morphological and electronic properties for Au thin film with 75 nm PMMA sublayer

Au thickness (nm)	Roughness (nm)	Grain size (nm)	Work function (eV)
15	50.145 ± 6.592	450 ± 20	4.748 ± 0.017
25	43.021 ± 3.685	325 ± 15	4.941 ± 0.012
35	46.250 ± 2.563	386 ± 19	4.869 ± 0.014

From the KPFM analysis, it is noted that all surfaces appear to exhibit regular nanosphere distributions. Tip shape effects are prominent in all three sample scans. It is further observed that there appears to be no trend with regards to the thickness of the Au film and the observed work function. This is particularly telling in the case of the 25 nm Au thick sample where the work function increases suddenly. Analysis

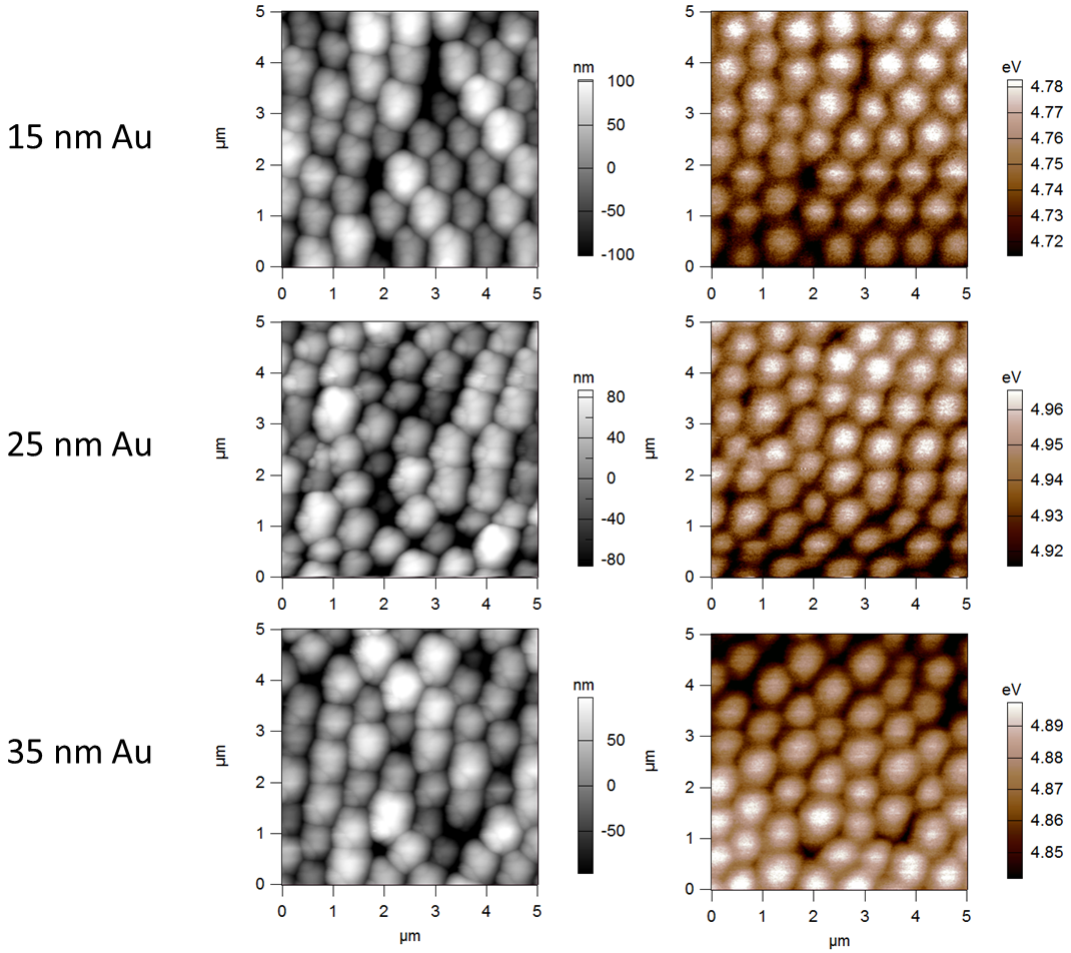

Figure 4.1: Height and work function maps of 15, 25 and 35 nm thick Au on 75 nm PMMA and 750 nm spheres

of the grain size indicates that in the particular case of the 75 nm thick PMMA, as grain size decreases, work function increases. This same trend is observed with respect to roughness and work function, demonstrating that grain size and roughness are related. Changes in work function with respect to grain size could be attributable to closer packing of spheres which would result in less inter sphere "filling" of Au and PMMA.

4.3.2 Au thin films morphological and electronic properties with 66 nm PMMA base layer

Work function and morphological parameters determinations were also performed on the analogous 66 nm thick PMMA samples. The resultant morphological and electronic maps are given in Figure 4.2, with the data summarized in Table 4.3.

Table 4.3: Morphological and electronic properties of Au thin film substrates prepared with 66 nm PMMA.

Au thickness (nm)	Roughness (nm)	Grain size (nm)	Work function (eV)
15	55.322 ± 8.371	482 ± 24	4.818 ± 0.026
25	44.453 ± 3.596	343 ± 15	4.821 ± 0.019
35	49.343 ± 5.980	475 ± 20	4.834 ± 0.019

Similar to the 75 nm PMMA samples, it is again noted that nanosphere distributions on the surface are regular and easily observed. Again, tip shape effects are prominent in the resultant imagery. In contrast to the results obtained from the 75 nm thick PMMA, the 66 nm thick PMMA shows some differing results. In the case of 66 nm PMMA, the observed work functions are all quite similar to one and other and are effectively the same within variance. This suggests that when 66 nm of PMMA is employed, changing the thickness of Au has little effect on the electronic properties of the substrate. Grain size and roughness are still affected by altering the thickness

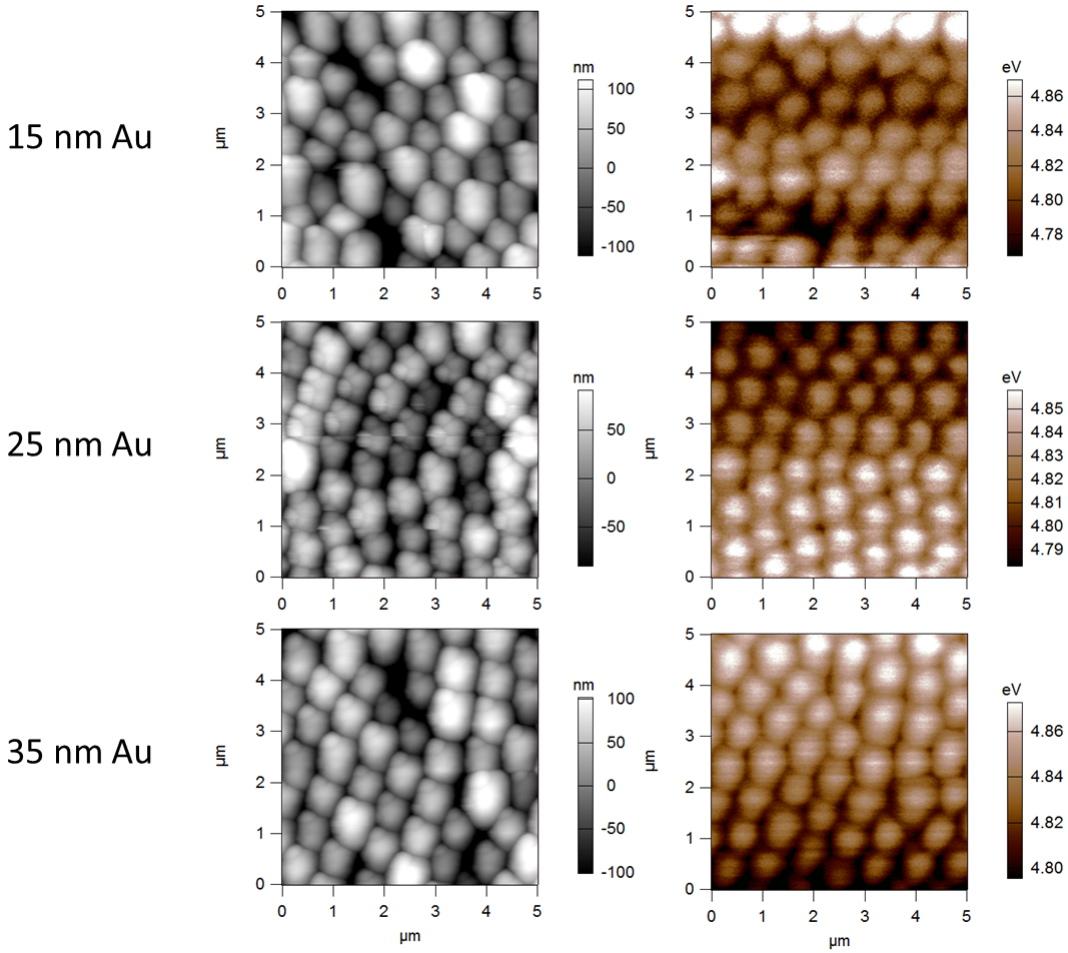

Figure 4.2: Height and work function maps of 15, 25 and 35 nm thick Au on 66 nm PMMA and 750 nm spheres

of Au and show the same trends as the 75 nm thick PMMA - a significant reduction in grain size and roughness occurs at 25 nm of Au. From both sets of samples, it is apparent that there is a significant effect present at 25 nm of Au that does not occur at 15 or 35 nm of Au. It is evident from these measurements that the thickness of PMMA plays a significant role in terms of the morphology of the substrate, however it does not affect the work function. From this, it is noted that the change in work function is not controlled by the morphology of the substrate. Again, these results must be compared to optical measurements to ascertain the specific role that this particular thickness of Au may play.

4.3.3 Mixed metal (Au/Ag) thin films morphological and electronic properties with 75 nm PMMA base layer

Samples of mixed metals (alternating Au and Ag) on 66 nm PMMA were also analyzed with KPFM to see how adjusting which metal layer is on the surface could effect the work function and resultant morphology. The morphological and work function maps are presented in Figure 4.3 and the data has been summarized in Table 4.4.

Table 4.4: KPFM analysis of samples prepared with 66 nm PMMA and alternating metal layers

Sample composition	Roughness (nm)	Grain size (nm)	Work function (eV)
15 nm Au on 10 nm Ag	43.783 ± 2.128	443 ± 17	4.833 ± 0.047
25 nm Au on 10 nm Ag	48.190 ± 2.868	422 ± 19	4.672 ± 0.027
15 nm Ag on 10 nm Au	49.017 ± 3.332	420 ± 16	4.781 ± 0.018
25 nm Ag on 10 nm Au	43.096 ± 4.727	394 ± 16	4.772 ± 0.032

Much like the single metal surfaces, the mixed metal samples also exhibit regular nanosphere distributions on the surface, with tip shape impacting the resultant images. It is observed that between 15 nm Au on 10 nm Ag and 25 nm Au on 10 nm Ag

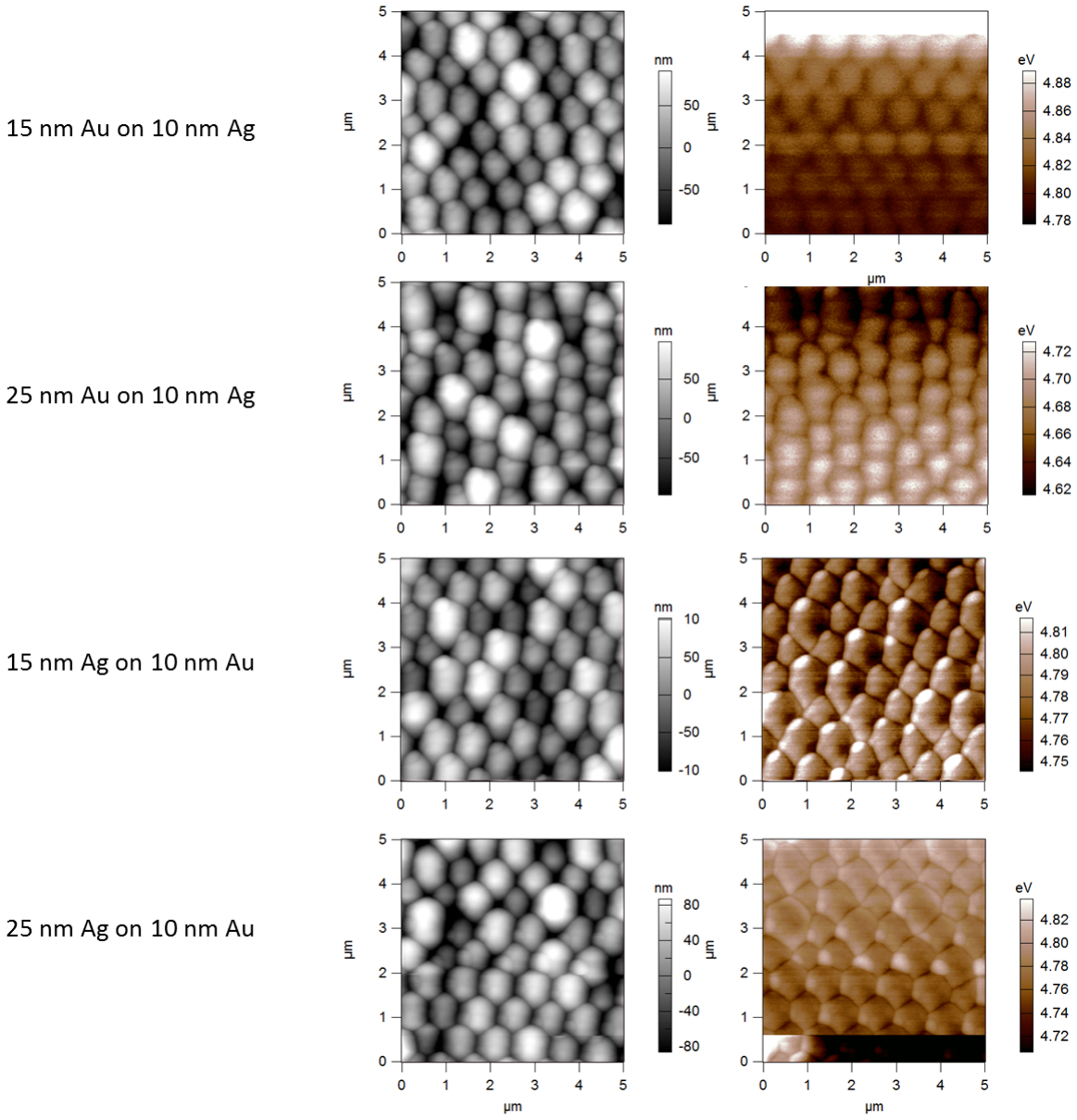

Figure 4.3: Height and work function maps of prepared combinations of Au/Ag and Ag/Au on 66 nm PMMA and 750 nm SiO_2 spheres

there is a significant change in the work function, again showing an overall decrease in the particular case of the 25 nm Au. This result is consistent with the measurements presented earlier in this section with only Au. It is worth noting that the grain size and roughness remain relatively constant with respect to one and other and do not show the overall decrease that was observed with just Au earlier in this section. This could be attributed to the fact that with the overall increased thickness of the substrate from the metal sublayer, the intersphere spacing has already been diminished. This "filling" could in turn affect the behavior of the capping metal layer such that its morphology is not as significantly influenced from the PMMA layer. This could be determined by successive x-ray diffraction (XRD) experiments on a range of sublayer metals and polymer thicknesses [95]. This would allow us to determine if the bulk crystal orientation of Au changes with sublayer thickness.

Overall the work function exhibits a decrease when the thickness of Au increases which is counter-intuitive, given that Ag has a lower work function than Au [96]. One would expect an overall increase as the thickness of Au increases, as the surface would exhibit more "gold like" characteristics. As previously proposed, successive XRD experiments could further elucidate the role that metal thickness plays with respect to the measured work function of the surfaces. This change in work function could be attributed to the emergence of differing Au crystal faces [97]. Combining XRD studies with KPFM would allow for a more accurate determination of the dominant crystal faces in our substrates and would provide key information to explain the work function measurements.

In the cases where Ag is forming the top layer of the surface, there is very little overall change in work function with variable Ag thickness. Grain size and roughness are relatively similar as well, which suggests little change between 15 nm and 25 nm Ag as the top layer. It is only in the particular case of Au as the top layer where we

observe significant changes with respect to thickness. Similar to the previous studies, comparing these results to optical measurements such as Raman spectroscopy and UV-Vis is critical to further understand the role that Au thickness plays in terms of surface and electronic properties.

4.4 Conclusion

We have demonstrated through KPFM measurements of the surfaces that all samples exhibit regular nanosphere distributions throughout. For the samples with 75 nm PMMA, an interesting trend is observed where work function increases as grain size decreases. This is not the case for the samples with 66 nm PMMA, where it is noted that work function remains constant regardless of Au thickness.

When Ag is introduced as a bottom layer with 66 nm PMMA, changes in work function are observed dependent on the thickness of the Au top layer. Specifically, the average work function of the 25 nm Au on 10 nm Ag sample is significantly lower than that of 15 nm Au on 10 nm Ag. From our measurements, it seems that there could be potential surface reconstruction occurring at 25 nm of Au. In the case of Ag forming the top layer, work function remains relatively constant regardless of Ag thickness which is contrary to the results we see with respect to Au in both the mixed metal case and the 75 nm PMMA case. In those particular instances, it is worth noting that overall sample thickness has increased. In the case of Au and 75 nm PMMA, overall sample thickness ranges from 80 nm to 110 nm. For the mixed metal samples, it is also noted that the sum thickness of the sample layers ranges from 89 nm to 109 nm however any changes in work function are only present when Au forms the top layer.

As previously mentioned, all of these results must be compared to Raman spectroscopic measurements and UV-Vis measurements to further understand the precise

role that Au thickness plays in terms of the observed electronic properties of these surfaces.

Chapter 5

Conclusions and Future Directions

5.1 Conclusions

5.1.1 Morphological considerations

The work performed in this thesis focused on novel surface enhanced Raman spectroscopy (SERS) substrates and their morphological and electronic characterization using Kelvin probe force microscopy (KPFM) [56]. In terms of linking morphology to the electronic properties, it was found that in terms of substrate morphological measurements there was very poor correlation between the observed roughness and grain size measurements to the electronic properties of the substrates themselves. This was evident in chapter 4 where it was discovered that the morphology of the substrates did not play a significant role in terms of the observed work functions. To truly determine the relationship that morphology has in terms of the electronic properties, it is suggested that these measurements be coupled with XRD results to determine how the electronic properties are changing with respect to changing crystal orientation. Similarly, it was found that there was very little correlation between morphological and electronic parameters measured for the Au/Cr systems presented in chapter 3.

It is important to mention that by controlling the thermal annealing temperatures of the substrates, it was possible to control the resultant morphological properties of the surfaces. Surface area measurements were employed to mitigate concentration effects of the analyte on the substrate so as to better represent the enhancement factors of the substrates.

5.1.2 Electronic property measurements

Electronic property measurements were undertaken as a significant portion of this thesis work to determine whether there was any correlation between both morphological and electronic properties, and subsequently to determine if any correlation exists between SERS measurements on phenanthrene and the electronic properties of these systems. As previously mentioned, in both chapters 3 and 4 there was no correlation between the observed morphological and electronic properties of the substrates, therefore controlling the electronic properties of a bulk substrate directly by altering the morphology was not possible with the methods described by this thesis.

This thesis further outlines a method for irradiating a SERS substrate and measuring the resultant work function of the system. It was determined that this new property, $p\phi$ is a critical property when considering the degree of SERS enhancement factor observed. Our data suggests that as $p\phi$ approaches the HOMO-LUMO energy of the target analyte, the EF^* reaches a maximum. Beyond the value of the analyte's HOMO-LUMO transition energy, EF^* decreases significantly. This suggests an energy matching regime between analyte and substrate which must be further explored and validated, however it remains an exciting result. This work has instilled optimism that the charge transfer between phenanthrene and substrate can potentially be observed *via* the photo-KPFM method outlined in chapter 3.

5.2 Future Directions

This thesis demonstrates that by studying the electronic properties of SERS substrates one can elucidate further information regarding the nature of its SERS activity. Furthermore, it is also clear that by controlling the morphology of the substrates the subsequent electronic properties will be altered to some degree which may also play a key role in determining the effectiveness of the resultant substrate.

In terms of further driving these particular projects forward, there is still a significant amount of work to be done. In particular, incorporating desorption ionisation mass spectrometry (DESI-MS) [93] into these studies will provide key information as to the amount of analyte adsorbed to the substrates. Specifically, DESI-MS is a surface ionisation technique which will allow for the desorption of any analyte of interest adsorbed to the SERS substrate. This will allow for the accurate preparation of SERS intensity calibration response curves to directly link the observed intensities in SERS measurements to the measured concentration of analytes adsorbed to the surface. To date, no such study has been investigated and this would be of key interest for determining the true response of a SERS substrate. This validation is critical to driving this project towards the ultimate goal of an integrated oil-in-water sensor.

For future sensor design and the elucidation of the exact role that work function plays in terms of charge transfer from substrate to analyte, computational modelling is paramount. The modelling of a sample surface (for example, a 4×4 square of Au atoms) in the vicinity of a phenanthrene molecule could reveal interesting computational data in terms of how the target analyte behaves in vicinity of the sample surface and how this would affect the simulated Raman spectrum and energies of this system. This is similar in idea to work presented by Chou [98] where they coupled SERS measurements to density functional theory (DFT) calculations of silver nanoparticles (AgNP's) as a sensing substrate for polyvinyl alcohol nanofibres. Through this com-

binatory method of investigating SERS systems, they were able to support their claim that the interaction which drives the SERS response was a result of the $-OH$ moiety on their target analyte. It is suggested that a similar approach be taken to determine the precise interaction of phenanthrene and a simple Au system before moving on to more complex systems such as those presented in this thesis work.

Appendix A

Calibration of Kelvin Probe Force Microscopy (KPFM) Tip

A.1 Highly oriented pyrolitic graphene (HOPG) as calibration substrate

KPFM relies on the idea that two metallic objects in near proximity to one another will behave as a parallel plate capacitor. As highly oriented pyrolitic graphite (HOPG) is metallic in nature and has a well known work function of 4.65 eV [99], it serves as a good calibration substrate for determining tip work function.

A.2 Experimental

KPFM images were acquired using a MFP-3D (Asylum Research) in SKPM mode. HOPG (Mikromasch) was freshly cleaved and imaged using a conductive Pt/Ti tip (Mikromasch, NSC35) with a nominal frequency of 145 kHz. The samples were placed on the ORCA (Asylum Research) sample holder with an Au clip connecting to sample.

A wire lead from the cantilever holder connects to a Au pad which in turn grounds the sample. All measurements were made at room temperature and atmospheric pressure. For a detailed schematic of this setup, refer to Section 3.2.2.3 from this thesis. All acquired images were 2.5 μm $\times$ 2.5 μm with 256 points per line, collected at a rate of 0.5 Hz. For the KPFM imagery, samples were at a 5 nm tip-sample separation during the second pass, as is standard in the literature [71, 100]. No image processing was applied to the KPFM imagery; a first order flatten procedure was applied to the height maps of the substrates. Average CPD values were collected from a 1.25 μm x 1.25 μm area centered on each image.

A.3 Results/Discussion

The tip work function was calculated by taking the average value of the CPD map of HOPG and then converting to tip work function by Eqn A.1:

$$eV_{CPD} = \phi_{tip} - \phi_{sample} \tag{A.1}$$

where e is elementary charge, ϕ_{tip} is the work function of the tip being calculated and ϕ_{sample} is the work function of the freshly cleaved HOPG substrate. This method results in a reliable method for determining tip work function.

A.4 Conclusions

KPFM measurements were made on freshly cleaved HOPG to determine the tip work function. This procedure serves as the most reliable and efficient method for determining the work function of the working KPFM probe/tip and is paramount for achieving accurate results during KPFM experiments.

Bibliography

[1] C. N. Banwell and E. M. McCash. *Fundamentals of Molecular Spectroscopy*. McGraw-Hill College, 4th revised edition, 1995.

[2] V. Resta, G. Quarta, M. Lomascolo, L. Maruccio, and L. Calcagnile. Raman and Photoluminescence spectroscopy of polycarbonate matrices irradiated with different energy $^{28}Si^{+}$ ions. *Vacuum*, 116:82–89, doi:10.1016/j.vacuum.2015.03.005.

[3] G. Barone, D. Bersani, J. Jehlička, P. P. Lottici, P. Mazzoleni, S. Raneri, P. Vandenabeele, C. Di Giacomo, and G. Larinà. Nondestructive investigation on the 17-18th centuries Sicilian jewelry collection at the Messina regional museum using mobile Raman equipment. *J. Raman Spectrosc.*, doi:10.1002/jrs.4649.

[4] A. Cesaratto, M. Leona, J. R. Lombardi, D. Comelli, A. Nevin, and P. Londero. Detection of organic colorants in historical painting layers using UV laser ablation surface-enhanced Raman microspectroscopy. *Angew. Chem. Int. Ed. Engl.*, 53(52):14373–7, doi:10.1002/anie.201408016.

[5] G. Perozziello, P. Candeloro, F. Gentile, M. L. Coluccio, M. Tallerico, A. De Grazia, A. Nicastri, A. M. Perri, E. Parrotta, F. Pardeo, R. Catalano, G. Cuda, and E. Di Fabrizio. A microfluidic dialysis device for complex biological mixture SERS analysis. *Microelectron. Eng.*, 144:37–41, doi:10.1016/j.mee.2015.02.015.

[6] A. Bohlin and C. J. Kliewer. Direct Coherent Raman Temperature Imaging and Wideband Chemical Detection in a Hydrocarbon Flat Flame. *J. Phys. Chem. Lett.*, 6(4):643–649, doi:10.1021/acs.jpclett.5b00014.

[7] M. J. Márquez, A. B. Brizuela, L. Davies, and S. A. Brandán. Spectroscopic and structural studies on lactose species in aqueous solution combining the HATR and Raman spectra with SCRF calculations. *Carbohydr. Res.*, 407C:34–41, doi:10.1016/j.carres.2015.01.019.

[8] I. J. Panneerdoss, S. J. Jeyakumar, S. Ramalingam, and M. Jothibas. Characterization of prepared In_2O_3 thin films: The FT-IR, FT-Raman, UV–Visible investigation and optical analysis. *Spectrochim. Acta Part A Mol. Biomol. Spectrosc.*, 147:1–13, doi:10.1016/j.saa.2015.02.033.

[9] R. Holze. The adsorption of thiophenol on gold - a spectroelectrochemical study. *Phys. Chem. Chem. Phys.*, doi:10.1039/c5cp00884k.

[10] C. V. Raman and K. S. Krishnan. A New Type of Secondary Radiation. *Nature*, 121(3048):501–502, doi:10.1038/121501c0.

[11] T. Rayleigh, R. Scattering, R. Spectroscopy, Q. Mechanics, and R. Spectra. *The Rayleigh and Raman Scattering,*, volume 30. Lawrence Radiation Laboratory, 1976.

[12] J. B. Jackson and N. J. Halas. Surface-enhanced Raman scattering on tunable plasmonic nanoparticle substrates. *Proc. Natl. Acad. Sci. U. S. A.*, 101(52):17930–17935, doi:10.1073/pnas.0408319102.

[13] G. L. Eesley. *Coherent Raman Spectroscopy*. Pergamon Press, Toronto, 1st edition, 1981.

[14] P. F. Mac-Millan. *Infrared and Raman Spectroscopy*, volume 18. Wiley-VCH Verlag GmbH, Weinheim, Germany, February 1988.

[15] P. F. Bernath. *Spectra of Atoms and Molecules*. Oxford University Press, New York, 2005.

[16] F. Reif. *Fundamentals of Statistical and Thermal Physics*. Waveland Press, Long Grove, IL, 1998.

[17] R. Petry, M. Schmitt, and J. Popp. Raman spectroscopy–a prospective tool in the life sciences. *ChemPhysChem*, 4(1):14–30, doi:10.1002/cphc.200390004.

[18] E. Li-Chan. The applications of Raman spectroscopy in food science. *Trends Food Sci. Technol.*, 7(11):361–370, doi:10.1016/S0924-2244(96)10037-6.

[19] B. Sharma, R. R. Frontiera, A.-I. Henry, E. Ringe, and R. P. Van Duyne. SERS: Materials, applications, and the future. *Mater. Today*, 15(1-2):16–25, doi:10.1016/S1369-7021(12)70017-2.

[20] J.-H. Yin, Z.-Y. Xiao, and Z.-W. Li. Ultralow concentration β-carotene molecule detection by liquid-core optical fiber resonance Raman spectroscopy. *Vib. Spectrosc.*, 62:7–9, doi:10.1016/j.vibspec.2012.05.014.

[21] M. Fleischmann, P. J. Hendra, and A. McQuillan. Raman spectra of pyridine adsorbed at a silver electrode. *Chem. Phys. Lett.*, 26(2):163–166, doi:10.1016/0009-2614(74)85388-1.

[22] P. L. Stiles, J. A. Dieringer, N. C. Shah, and R. P. Van Duyne. Surface-enhanced Raman spectroscopy. *Annu. Rev. Anal. Chem. (Palo Alto. Calif).*, 1:601–626, doi:10.1146/annurev.anchem.1.031207.112814.

[23] M. G. Albrecht and J. A. Creighton. Anomalously intense Raman spectra of pyridine at a silver electrode. *J. Am. Chem. Soc.*, 99(15):5215–5217, doi:10.1021/ja00457a071.

[24] D. L. Jeanmaire and R. P. Van Duyne. Surface Raman spectroelectrochemistry. *J. Electroanal. Chem. Interfacial Electrochem.*, 84(1):1–20, doi:10.1016/S0022-0728(77)80224-6.

[25] L. Li, T. Hutter, U. Steiner, and S. Mahajan. Single molecule SERS and detection of biomolecules with a single gold nanoparticle on a mirror junction. *Analyst*, 138(16):4574–8, doi:10.1039/c3an00447c.

[26] D. Lis and F. Cecchet. Localized surface plasmon resonances in nanostructures to enhance nonlinear vibrational spectroscopies: towards an astonishing molecular sensitivity. *Beilstein J. Nanotechnol.*, 5(1):2275–92, doi:10.3762/bjnano.5.237.

[27] B. Cooper, H. Ehrenreich, and H. Philipp. Optical Properties of Noble Metals. II. *Phys. Rev.*, 138(2A):A494–A507, doi:10.1103/PhysRev.138.A494.

[28] Y.-L. Liu, C.-Y. Fang, C.-C. Yu, T.-C. Yang, and H.-L. Chen. Controllable Localized Surface Plasmonic Resonance Phenomena in Reduced Gold Oxide Films. *Chem. Mater.*, 26(5):1799–1806, doi:10.1021/cm403227w.

[29] T. Dörfer, M. Schmitt, and J. Popp. Deep-UV surface-enhanced Raman scattering. *J. Raman Spectrosc.*, 38(11):1379–1382, doi:10.1002/jrs.1831.

[30] A. Campion and P. Kambhampati. Surface-enhanced Raman scattering. *Chem. Soc. Rev.*, 27(4):241, doi:10.1039/a827241z.

[31] I. López-Tocón, J. C. Otero, J. F. Arenas, J. V. Garcia-Ramos, and S. Sanchez-Cortes. Multicomponent direct detection of polycyclic aromatic hydrocarbons by surface-enhanced Raman spectroscopy using silver nanoparticles functionalized with the viologen host lucigenin. *Anal. Chem.*, 83(7):2518–25, doi:10.1021/ac102771w.

[32] P. Leyton, I. Córdova, P. Lizama-Vergara, J. Gómez-Jeria, A. Aliaga, M. Campos-Vallette, E. Clavijo, J. García-Ramos, and S. Sanchez-Cortes. Humic acids as molecular assemblers in the surface-enhanced Raman scattering detection of polycyclic aromatic hydrocarbons. *Vib. Spectrosc.*, 46(2):77–81, doi:10.1016/j.vibspec.2007.10.006.

[33] P. Leyton, J. S. Gómez-Jeria, S. Sanchez-Cortes, C. Domingo, and M. Campos-Vallette. Carbon nanotube bundles as molecular assemblies for the detection of polycyclic aromatic hydrocarbons: surface-enhanced resonance Raman spectroscopy and theoretical studies. *J. Phys. Chem. B*, 110(13):6470–4, doi:10.1021/jp056379z.

[34] Y.-H. Kwon, K. Sowoidnich, H. Schmidt, and H.-D. Kronfeldt. Application of calixarene to high active surface-enhanced Raman scattering (SERS) substrates suitable for in situ detection of polycyclic aromatic hydrocarbons (PAHs) in seawater. *J. Raman Spectrosc.*, 43(8):1003–1009, doi:10.1002/jrs.3157.

[35] X. Shi, J. Ma, R. Zheng, C. Wang, and H.-D. Kronfeldt. An improved self-assembly gold colloid film as surface-enhanced Raman substrate for detection of trace-level polycyclic aromatic hydrocarbons in aqueous solution. *J. Raman Spectrosc.*, 43(10):1354–1359, doi:10.1002/jrs.4062.

[36] J. Pfannkuche, L. Lubecki, H. Schmidt, G. Kowalewska, and H. D. Kronfeldt. The use of surface-enhanced Raman scattering (SERS) for detection of PAHs in the Gulf of Gdańsk (Baltic Sea). *Mar. Pollut. Bull.*, 64(3):614–626, doi:10.1016/j.marpolbul.2011.12.008.

[37] H. Zhao, J. Jin, W. Tian, R. Li, Z. Yu, W. Song, Q. Cong, B. Zhao, and Y. Ozaki. Three-dimensional superhydrophobic surface-enhanced Raman spectroscopy substrate for sensitive detection of pollutants in real environments. *J. Mater. Chem. A*, 3(8):4330–4337, doi:10.1039/C4TA06590E.

[38] Y. Xie, X. Wang, X. Han, W. Song, W. Ruan, J. Liu, B. Zhao, and Y. Ozaki. Selective SERS detection of each polycyclic aromatic hydrocarbon (PAH) in a mixture of five kinds of PAHs. *J. Raman Spectrosc.*, 42(5):945–950, doi:10.1002/jrs.2818.

[39] J. Chen, Y.-W. Huang, and Y. Zhao. Characterization of polycyclic aromatic hydrocarbons using Raman and surface-enhanced Raman spectroscopy. *J. Raman Spectrosc.*, 46(1):64–69, doi:10.1002/jrs.4612.

[40] J. Chen, Y.-W. Huang, and Y. Zhao. Detection of polycyclic aromatic hydrocarbons from cooking oil using ultra-thin layer chromatography and surface enhanced Raman spectroscopy. *J. Mater. Chem. B*, 3(9):1898–1906, doi:10.1039/C4TB01632G.

[41] X. Wang, W. Hao, H. Zhang, Y. Pan, Y. Kang, X. Zhang, M. Zou, P. Tong, and Y. Du. Analysis of polycyclic aromatic hydrocarbons in water with gold nanoparticles decorated hydrophobic porous polymer as surface-enhanced Raman spectroscopy substrate. *Spectrochim. Acta. A. Mol. Biomol. Spectrosc.*, 139:214–21, doi:10.1016/j.saa.2014.11.104.

[42] A. M. Fales, H. Yuan, and T. Vo-Dinh. Development of Hybrid Silver-Coated Gold Nanostars for Nonaggregated Surface-Enhanced Raman Scattering. *J. Phys. Chem. C. Nanomater. Interfaces*, 118(7):3708–3715, doi:10.1021/jp4091393.

[43] H. T. Ngo, H.-N. Wang, T. Burke, G. S. Ginsburg, and T. Vo-Dinh. Multiplex detection of disease biomarkers using SERS molecular sentinel-on-chip. *Anal. Bioanal. Chem.*, 406(14):3335–44, doi:10.1007/s00216-014-7648-4.

[44] H. T. Ngo, H.-N. Wang, A. M. Fales, B. P. Nicholson, C. W. Woods, and T. Vo-Dinh. DNA bioassay-on-chip using SERS detection for dengue diagnosis. *Analyst*, 139(22):5655–9, doi:10.1039/c4an01077a.

[45] K. V. Kong, W. K. Leong, Z. Lam, T. Gong, D. Goh, W. K. O. Lau, and M. Olivo. A Rapid and Label-free SERS Detection Method for Biomarkers in Clinical Biofluids. *Small*, 10(24):5030–5034, doi:10.1002/smll.201401713.

[46] C. L. Wong, U. S. Dinish, K. D. Buddharaju, M. S. k. Schmidt, and M. Olivo. Surface-enhanced Raman scattering (SERS)-based volatile organic compounds (VOCs) detection using plasmonic bimetallic nanogap substrate. *Appl. Phys. A*, 117(2):687–692, doi:10.1007/s00339-014-8723-6.

[47] Y. Liu, J. Zhou, B. Wang, T. Jiang, H.-P. Ho, L. Petti, and P. Mormile. Au@Ag core-shell nanocubes: epitaxial growth synthesis and surface-enhanced Raman scattering performance. *Phys. Chem. Chem. Phys.*, 17(10):6819–26, doi:10.1039/c4cp05642f.

[48] Q. W. Huang, J. Zhang, A. Berlie, Z. X. Qin, X. M. Zhao, J. B. Zhang, L. Y. Tang, J. Liu, C. Zhang, G. H. Zhong, H. Q. Lin, and X. J. Chen. Structural

and vibrational properties of phenanthrene under pressure. *J. Chem. Phys.*, 139(10):104302, doi:10.1063/1.4820359.

[49] G. Binnig and C. F. Quate. Atomic Force Microscope. *Phys. Rev. Lett.*, 56(9):930–933, doi:10.1103/PhysRevLett.56.930.

[50] R. V. Lapshin. Analytical model for the approximation of hysteresis loop and its application to the scanning tunneling microscope. *Rev. Sci. Instrum.*, 66(9):4718–4730, doi:10.1063/1.1145314.

[51] NT-MDT. Calibration of the optical detection system.

[52] E. Sprague, J. C. Palmaz, C. Simon, and A. Watson. Electrostatic forces on the surface of metals as measured by atomic force microscopy. *J. Long. Term. Eff. Med. Implants*, 10(1-2):111–125, doi:10.1615/.v10.i12.100.

[53] Q. Zhong, D. Inniss, K. Kjoller, and V. Elings. Fractured polymer/silica fiber surface studied by tapping mode atomic force microscopy. *Surf. Sci. Lett.*, 290(1-2):L688–L692, doi:10.1016/0167-2584(93)90906-Y.

[54] R. García and A. San Paulo. Attractive and repulsive tip-sample interaction regimes in tapping-mode atomic force microscopy. *Phys. Rev. B*, 60(7):4961–4967, doi:10.1103/PhysRevB.60.4961.

[55] I. Schmitz, M. Schreiner, G. Friedbacher, and M. Grasserbauer. Tapping-Mode AFM in Comparison to Contact-Mode AFM as a Tool for in Situ Investigations of Surface Reactions with Reference to Glass Corrosion. *Anal. Chem.*, 69(6):1012–1018, doi:10.1021/ac9607020.

[56] M. Nonnenmacher, M. P. O'Boyle, and H. K. Wickramasinghe. Kelvin probe force microscopy. *Appl. Phys. Lett.*, 58(25):2921–2923, doi:10.1063/1.105227.

[57] R. Smoluchowski. Anisotropy of the electronic work function of metals. *Phys. Rev.*, 60(9):661–674, doi:10.1103/PhysRev.60.661.

[58] W. Melitz, J. Shen, A. C. Kummel, and S. Lee. Kelvin probe force microscopy and its application. *Surf. Sci. Rep.*, 66(1):1–27, doi:10.1016/j.surfrep.2010.10.001.

[59] M. M. Giangregorio, M. Losurdo, G. V. Bianco, A. Operamolla, E. Dilonardo, A. Sacchetti, P. Capezzuto, F. Babudri, and G. Bruno. Insight into gold nanoparticle-hydrogen interaction: A way to tailor nanoparticle surface charge and self-assembled monolayer chemisorption. *J. Phys. Chem. C*, 115(40):19520–19528, doi:10.1021/jp2054525.

[60] F. N. Afshar, A. M. Glenn, J. H. W. De Wit, H. Terryn, and J. M. C. Mol. A combined electron probe micro analysis and scanning Kelvin probe force microscopy study of a modified AA4xxx/AA3xxx aluminium brazing sheet. *Electrochim. Acta*, 104:48–63, doi:10.1016/j.electacta.2013.04.080.

[61] F. N. Afshar, J. H. W. De Wit, H. Terryn, and J. M. C. Mol. Scanning Kelvin probe force microscopy as a means of predicting the electrochemical characteristics of the surface of a modified AA4xxx/AA3xxx (Al alloys) brazing sheet. *Electrochim. Acta*, 88:330–339, doi:10.1016/j.electacta.2012.10.051.

[62] P. Premendra, H. Terryn, J. M. C. Mol, J. H. W. De Wit, and L. Katgerman. A comparative electrochemical study of commercial and model aluminium alloy (AA5050). *Mater. Corros.*, 60(6):399–406, doi:10.1002/maco.200805145.

[63] T. Pan. Intrinsically Conducting Polymer-Based Heavy-Duty and Environmentally Friendly Coating System for Corrosion Protection of Structural Steels. *Spectrosc. Lett.*, 46(4):268–276, doi:10.1080/00387010.2012.725235.

[64] T. Pan. Stressed Corrosion of an Austenitic Stainless Steel Studied by Scanning Kelvin Probe Force Microscopy. *Anal. Lett.*, 45(17):2580–2588, doi:10.1080/00032719.2012.694944.

[65] F. Andreatta, M. E. Druart, E. Marin, D. Cossement, M. G. Olivier, and L. Fedrizzi. Volta potential of clad AA2024 aluminium after exposure to $CeCl_3$ solution. *Corros. Sci.*, 86:189–201, doi:10.1016/j.corsci.2014.05.008.

[66] E. Marin, M. Lekka, F. Andreatta, L. Fedrizzi, G. Itskos, A. Moutsatsou, N. Koukouzas, and N. Kouloumbi. Electrochemical study of Aluminum-Fly Ash composites obtained by powder metallurgy. *Mater. Charact.*, 69:16–30, doi:10.1016/j.matchar.2012.04.004.

[67] A. Stadler. Transparent Conducting Oxides—An Up-To-Date Overview. *Materials (Basel).*, 5(12):661–683, doi:10.3390/ma5040661.

[68] G. De Luca, A. Liscio, G. Battagliarin, L. Chen, L. M. Scolaro, K. Müllen, P. Samorì, and V. Palermo. Orthogonal self-assembly and selective solvent vapour annealing: simplified processing of a photovoltaic blend. *Chem. Commun. (Camb).*, 49(39):4322–4, doi:10.1039/c2cc37909k.

[69] A. Liscio, V. Palermo, and P. Samorì. Nanoscale quantitative measurement of the potential of charged nanostructures by electrostatic and Kelvin probe force microscopy: Unraveling electronic processes in complex materials. *Acc. Chem. Res.*, 43(4):541–550, doi:10.1021/ar900247p.

[70] A. Liscio, G. De Luca, F. Nolde, V. Palermo, K. Müllen, and P. Samorì. Photovoltaic charge generation visualized at the nanoscale: A proof of principle. *J. Am. Chem. Soc.*, 130(3):780–781, doi:10.1021/ja075291r.

[71] S. Sadewasser, D. Abou-Ras, D. Azulay, R. Baier, I. Balberg, D. Cahen, S. Cohen, K. Gartsman, K. Ganesan, J. Kavalakkatt, W. Li, O. Millo, T. Rissom, Y. Rosenwaks, H. W. Schock, a. Schwarzman, and T. Unold. Nanometer-scale electronic and microstructural properties of grain boundaries in Cu(In,Ga)Se_2. *Thin Solid Films*, 519(21):7341–7346, doi:10.1016/j.tsf.2010.12.227.

[72] R. Mainz, F. Streicher, D. Abou-Ras, S. Sadewasser, R. Klenk, and M. C. Lux-Steiner. Combined analysis of spatially resolved electronic structure and composition on a cross-section of a thin film Cu($In_{1-x}Ga_x$)S_2 solar cell. *Phys. status solidi*, 206(5):1017–1020, doi:10.1002/pssa.200881216.

[73] M. Takihara, T. Minemoto, Y. Wakisaka, and T. Takahashi. An investigation of band profile around the grain boundary of Cu(In_Ga)Se_2 solar cell material by scanning probe microscopy. *Prog. Photovoltaics Res. Appl.*, 21:595–599, doi:10.1002/pip.1235.

[74] T. Takahashi. Photoassisted Kelvin probe force microscopy on multicrystalline Si solar cell materials. *Jpn. J. Appl. Phys.*, 50(8):08LA05, doi:10.1143/JJAP.50.08LA05.

[75] K. Hara and T. Takahashi. Photothermal signal and surface potential around grain boundaries in multicrystalline silicon solar cells investigated by scanning probe microscopy. *Appl. Phys. Express*, 5(2):022301, doi:10.1143/APEX.5.022301.

[76] K. Lee and J. Neff, editors. *Produced Water*. Springer New York, New York, NY, 2011.

[77] T. Gutierrez. Identifying polycyclic aromatic hydrocarbon-degrading bacteria in oil-contaminated surface waters at Deepwater Horizon by cultivation, stable

isotope probing and pyrosequencing. *Rev. Environ. Sci. Biotechnol.*, 10(4):301–305, doi:10.1007/s11157-011-9252-9.

[78] J. F. Collins, J. P. Brown, G. V. Alexeeff, and A. G. Salmon. Potency equivalency factors for some polycyclic aromatic hydrocarbons and polycyclic aromatic hydrocarbon derivatives. *Regul. Toxicol. Pharmacol.*, 28(1):45–54, doi:10.1006/rtph.1998.1235.

[79] U.S. Environmental Protection Agency. Ambient Water Quality Criteria for Polynuclear Aromatic Hydrocarbons. Technical report, BC Ministry of Environment, Victoria, 1980.

[80] B. Moazzez. *An experimental and computational approach to the development of SERS substrates for water quality monitoring sensors*. Ph.d, Memorial University of Newfoundland, 2015.

[81] T. Takahashi, H. Tokailin, and T. Sagawa. Angle-resolved ultraviolet photoelectron spectroscopy of the unoccupied band structure of graphite. *Phys. Rev. B*, 32(12):8317–8324, doi:10.1103/PhysRevB.32.8317.

[82] D. Nečas and P. Klapetek. Gwyddion: an open-source software for SPM data analysis. *Cent. Eur. J. Phys.*, 10(1):181–188, doi:10.2478/s11534-011-0096-2.

[83] F. Hubenthal, D. Blázquez Sánchez, N. Borg, H. Schmidt, H.-D. Kronfeldt, and F. Träger. *Appl. Phys. B*, 95(2):351–359, doi:10.1007/s00340-009-3373-7.

[84] B. Bhushan. *Modern Tribology Handbook, Two Volume Set*. CRC Press, 2000.

[85] L. Vincent and P. Soille. Watersheds in digital spaces: An efficient algorithm based on immersion simulations. *IEEE Trans. Pattern Anal. Mach. Intell.*, 13(6):583–598, doi:10.1109/34.87344.

[86] V. L. De Los Santos, D. Lee, J. Seo, F. L. Leon, D. A. Bustamante, S. Suzuki, Y. Majima, T. Mitrelias, A. Ionescu, and C. H. W. Barnes. Crystallization and surface morphology of Au/SiO_2 thin films following furnace and flame annealing. *Surf. Sci.*, 603(19):2978–2985, doi:10.1016/j.susc.2009.08.011.

[87] J. Huang, Y. Zhu, M. Lin, Q. Wang, L. Zhao, Y. Yang, K. X. Yao, and Y. Han. Site-specific growth of Au-Pd alloy horns on Au nanorods: a platform for highly sensitive monitoring of catalytic reactions by surface enhancement Raman spectroscopy. *J. Am. Chem. Soc.*, 135(23):8552–61, doi:10.1021/ja4004602.

[88] S. Karim, M. E. Toimil-Molares, A. G. Balogh, W. Ensinger, T. W. Cornelius, E. U. Khan, and R. Neumann. Morphological evolution of Au nanowires controlled by Rayleigh instability. *Nanotechnology*, 17(24):5954–5959, doi:10.1088/0957-4484/17/24/009.

[89] Y. Zhao, X. Liu, D. Y. Lei, and Y. Chai. Effects of surface roughness of Ag thin films on surface-enhanced Raman spectroscopy of graphene: spatial nonlocality and physisorption strain. *Nanoscale*, 6(3):1311–7, doi:10.1039/c3nr05303b.

[90] E. C. Le Ru, E. Blackie, M. Meyer, and P. G. Etchegoin. Surface enhanced raman scattering enhancement factors: A comprehensive study. *J. Phys. Chem. C*, 111(37):13794–13803, doi:10.1021/jp0687908.

[91] G. Malloci, G. Cappellini, G. Mulas, and A. Mattoni. Electronic and optical properties of families of polycyclic aromatic hydrocarbons: A systematic (time-dependent) density functional theory study. *Chem. Phys.*, 384(1-3):19–27, doi:10.1016/j.chemphys.2011.04.013.

[92] H. B. Klevens. Spectral Resemblances between Azulenes and Their Corresponding Six-Carbon Ring Isomers. *J. Chem. Phys.*, 18(8):1063, doi:10.1063/1.1747858.

[93] Z. Takáts, J. M. Wiseman, B. Gologan, and R. G. Cooks. Mass spectrometry sampling under ambient conditions with desorption electrospray ionization. *Science*, 306(5695):471–3, doi:10.1126/science.1104404.

[94] MicroChem. NANO PMMA and Copolymer ™, 2001.

[95] P. Yang, H. Yan, S. Mao, R. Russo, J. Johnson, R. Saykally, N. Morris, J. Pham, R. He, and H.-J. Choi. Controlled Growth of ZnO Nanowires and Their Optical Properties. *Adv. Funct. Mater.*, 12(5):323, doi:10.1002/1616-3028(20020517)12:5<323::AID-ADFM323>3.0.CO;2-G.

[96] S. Halas and T. Durakiewicz. Work functions of elements expressed in terms of the Fermi energy and the density of free electrons. *J. Phys. Condens. Matter*, 10(48):10815–10826, doi:10.1088/0953-8984/10/48/005.

[97] S. Sadewasser. Surface potential of chalcopyrite films measured by KPFM. *Phys. Status Solidi*, 203(11):2571–2580, doi:10.1002/pssa.200669573.

[98] H. L. Chou, C. M. Wu, F. D. Lin, and J. Rick. Interactions between silver nanoparticles and polyvinyl alcohol nanofibers. *AIP Adv.*, 4(8):087111, doi:10.1063/1.4890290.

[99] V. Palermo, M. Palma, v. Tomović, M. D. Watson, R. Friedlein, K. Müllen, and P. Samorì. Influence of molecular order on the local work function of nanographene architectures: A Kelvin-probe force microscopy study. *ChemPhysChem*, 6(11):2371–2375, doi:10.1002/cphc.200500181.

[100] L. Z. Borg, A. L. Domanski, A. Breivogel, M. Bürger, R. Berger, K. Heinze, and R. Zentel. Light-induced charge separation in a donor–chromophore–acceptor nanocomposite poly[TPA−$Ru(tpy)_2$]@ZnO. *J. Mater. Chem. C*, 1(6):1223–1230, doi:10.1039/C2TC00535B.